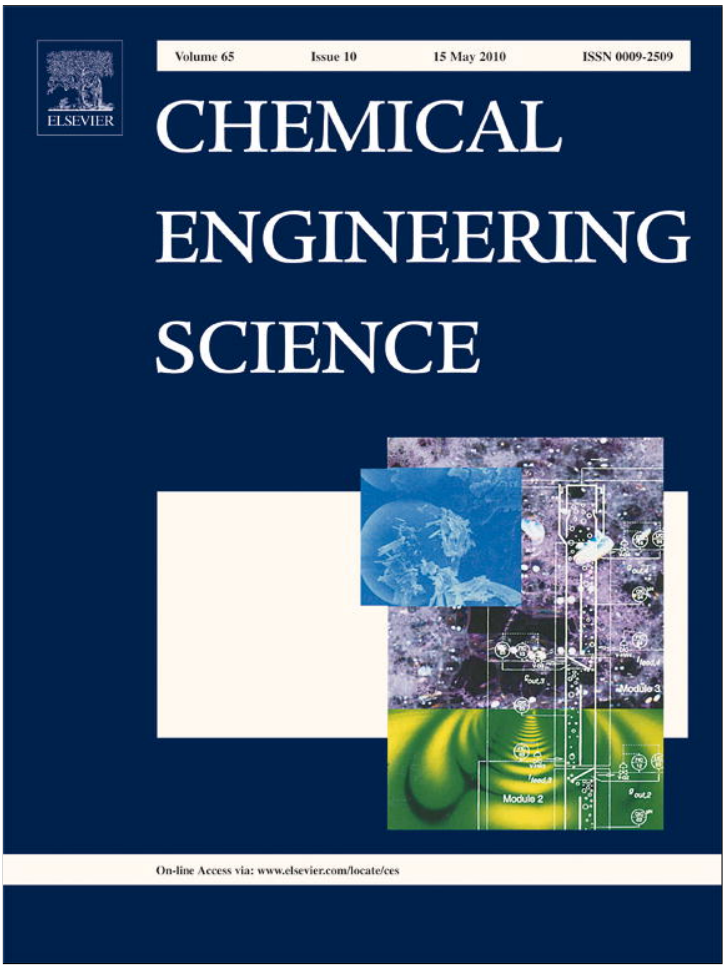

Chemical Engineering Science 65 (2010) 2934–2956

Contents lists available at ScienceDirect

Chemical Engineering Science

journal homepage: www.elsevier.com/locate/ces

Numerical simulation of mass transfer in circulating drops

S. Ubal, C.H. Harrison, P. Grassia *, W.J. Korchinsky

CEAS, University of Manchester, PO Box 88, Sackville St., Manchester M60 1QD, UK

ARTICLE INFO

Article history:
Received 15 October 2009
Received in revised form
19 January 2010
Accepted 20 January 2010
Available online 25 January 2010

Keywords:
Mass transfer
Circulating drop model
Convective transport
High Peclet number
Cross-stream diffusion
Boundary layers
Mathematical modelling
Numerical analysis
Simulation
Liquid–liquid extraction

ABSTRACT

Numerical simulations of mass transfer are performed for a circulating liquid drop with applications in liquid–liquid extraction. Simulation parameters are chosen for a multi-component ternary system acetone–methanol–benzene. The drop circulation pattern is estimated via a truncated Galerkin representation of the drop streamfunction. Fickian diffusivities for multi-component mass transfer are obtained via Maxwell–Stefan theory with thermodynamic corrections. The advection–diffusion equations governing mass transfer are solved via two distinct numerical methods: a finite difference scheme (using the alternating direction implicit method) and a finite element scheme. Good agreement was obtained between both schemes. Simulation results are presented for a Reynolds number ($Re=30$) and for a selection of Peclet numbers ($Pe=100$, 1000 and 10 000, thereby giving insight into the effects of increasing Peclet number). The numerical simulations of the full advection–diffusion equations are compared against predictions of a rigid drop model (i.e. without circulation) and also against predictions of a semi-analytical boundary layer model developed by Uribe-Ramirez and Korchinsky. Results for bulk mass fractions reveal that the rigid drop model predictions evolve too slowly, while the boundary layer model predictions evolve much more quickly than the numerical simulations. Advection–diffusion simulation results for the evolution of mass fractions at selected individual locations in the drop show that points on streamlines nearest to the drop surface and/or drop axis evolve fastest, while those closest to the drop internal stagnation point evolve slowest. Corroborated by contour plots of component concentrations throughout the drop at selected times, this supports a picture whereby mass fractions become roughly uniform along individual streamlines, but mass is transferred diffusively from streamline to streamline.

1. Introduction

Mass transfer via liquid–liquid extraction is an important chemical engineering operation in many processes (van Vliet et al., 2001; Li et al., 2002a; Chambliss et al., 2002; Alonso et al., 2007). Liquid–liquid extraction proceeds by suspending a dispersed phase of liquid droplets (solvent plus solute) in a continuous phase of another immiscible liquid (again solvent plus solute). Solute transfers down concentration gradients (or strictly down gradients of chemical potential, Taylor and Krishna, 1993; Klocker et al., 1997) from the dispersed to the continuous phase or vice versa.

Good physical understanding of these mass transfer processes is essential for robustly designing a liquid–liquid extraction system. There have been many research efforts toward this end, including theories for predicting solute diffusivities (often in systems with multiple components) (Kooijman and Taylor, 1991; Wesselingh and Krishna, 1991; Bandrowski and Kubaczka, 1982), predictions of mass transfer coefficients (Kumar and Hartland, 1999; Handlos and Baron, 1957; Kronig and Brink, 1950), CFD simulations of droplet motion in feasible/realistic extraction system geometries (Piarah et al., 2001; Vikhansky and Kraft, 2004; Drumm et al., 2008, 2009), and population balance mass transfer models for swarms of droplets (Vikhansky and Kraft, 2004; Drumm et al., 2009; Goodson and Kraft, 2004; Toutain et al., 1998).

However, it is fair to say that even the mass transfer process on the scale of a single drop is not fully understood. Drops dispersed in liquid–liquid extraction systems are generally not rigid entities: instead circulation patterns are set up internal to and external to the drop (Kumar and Hartland, 1999; Kronig and Brink, 1950; Juncu, 1999). These circulation patterns convert the mass transfer process from a purely diffusive one, to an advective–diffusive process (Juncu, 2001, 2005), leading to a considerable complication in the spatiotemporal distribution of solute. Ideally one would want to gain an in depth understanding of these (quite complicated) single drop processes, and incorporate that understanding into larger scale modelling and design of liquid–liquid extraction systems (containing a multitude of drops).

* Corresponding author. Tel.: +44 161 306 8851; fax: +44 161 306 9321.
E-mail address: paul.grassia@manchester.ac.uk (P. Grassia).

0009-2509/$ - see front matter © 2010 Elsevier Ltd. All rights reserved.
doi:10.1016/j.ces.2010.01.021

The present work aims to study the single drop mass transfer process at a greater level of detail than has been achieved hitherto. Towards this end, a numerical simulation of the advection–diffusion processes in a single drop has been developed/analysed. Some of the previously proposed models (Uribe-Ramirez and Korchinsky, 2000a, b; Negri and Korchinsky, 1986; Negri et al., 1986) for mass transfer on the drop scale will be found to over- or under-predict the mass transfer rates compared to the full numerical simulation. The scale of one previous model's overprediction (in particular that of Uribe-Ramirez and Korchinsky, 2000a, b) is very large indeed—mass transfer predictions could be up to the order of 10 times more rapid with the previous model compared to the present simulations. The reasons for this discrepancy turn out to be insightful, and are explained in depth.

This paper is laid out as follows. Section 2 reviews mass transfer and fluid flow for single drops. Section 3 develops the equations describing mass transfer. Numerical methods for solving the equations are given in Section 4. Results are presented in Section 5, whilst Sections 6 and 7 offer discussion and conclusions. Technical and mathematical details of the analysis are relegated to appendices.

2. Review of single drop mass transfer and fluid flow

This section is laid out as follows. Section 2.1 reviews mass transfer in drops which are effectively rigid entities, whereby mass transfer is wholly diffusive. Section 2.2 reviews circulation patterns in and around drops. Then Section 2.3 treats advective–diffusive mass transfer in drops in the presence of circulation.

2.1. Mass transfer in rigid drops

It is simplest to consider mass transfer to and from a spherical drop in the case where there is no fluid circulation (Newman, 1931). Mass transfer is then wholly radial, and analytic solutions are available to describe the solute concentration field as a function of radial coordinate. There are two distinct analytical approaches.

One is a separation of variables technique (Negri and Korchinsky, 1986; Negri et al., 1986). Given an initial mass fraction of solute in the drop and a different mass fraction imposed externally and/or on the boundary, the separation of variables solution describes the solute concentration field as a product of a radial function and a temporal function (or strictly speaking as an infinite sum of such products). The radial functions give a Fourier series representation of the instantaneous concentration field, while the temporal functions describe exponential decay.

The higher Fourier modes have faster temporal decay rates, so that (at long times) relatively few Fourier modes survive. At early times, however, increasing numbers of Fourier modes must be considered. Indeed, at extremely early times, changes in the solute concentration field (compared to the initial concentration field) are confined to a relatively thin layer of material near the drop surface: large numbers of Fourier modes need to be included to resolve these thin layers. Under such circumstances one is prompted to search for a more efficient/compact analytical description of the solute field.

The second analytical approach (Bird et al., 1960) therefore applies at sufficiently early times, when (as far as gradients of solute concentration are concerned), the drop surface looks locally flat. One-dimensional diffusion models can then be applied. So-called similarity solutions for the solute concentration field then arise, expressed in terms of distance from the drop surface and time.

The thickness of the layer (to which concentration gradients are confined) grows proportional to the square root of time. A similarity variable can be defined as a ratio between two distances: the distance of a coordinate point from the drop surface, and the growing layer thickness. Expressed in terms of this similarity variable, the solute concentration field takes the form of an error function: this interpolates between the initial solute concentration and the surface concentration. The similarity form of the solution breaks down when the layer thickness grows to a significant fraction of the drop radius: at this point the similarity solution should be abandoned.

The above discussion concerned a rigid drop. The key change occurring in the presence of circulation is that the solute concentration field depends on (polar) angle as well as radial coordinate and time (Kronig and Brink, 1950; Juncu, 2001, 2005; Chao and Chen, 1970). Understanding the circulation pattern is essential first, before analysing mass transfer with circulation. Thus circulation patterns are treated in the next subsection.

2.2. Circulation patterns in and around drops

We suppose that the drop shape remains spherical despite the circulation. As drop sizes and/or velocities grow, drops deviate from sphericity (and their shape may even become oscillatory/unsteady with respect to time) (Yang and Mao, 2005; Li et al., 2002b; Dandy and Leal, 1989; Rose and Kintner, 1966): such complications are ignored here. Instead we restrict attention to steady state, laminar and axisymmetric circulation fields within and around a spherical circulating drop. Note, however, that while the flow fields here are at steady state, the solute concentration fields are unsteady. Flow fields are assumed independent of the solute concentration fields (but certainly not vice versa).

Solving for the flow fields in and around a moving spherical liquid drop is a well-posed fluid mechanics problem (Batchelor, 1967). The flow satisfies momentum and continuity equations, as well as boundary conditions, on velocities and tangential viscous stresses at the drop surface. In the frame of the drop, the flow field must also asymptote to a uniform translational motion at large distances. The parameters affecting the flow are the ratio between internal and external densities, the ratio between internal and external viscosities, and the Reynolds number (either the internal or external Reynolds number is sufficient, since one can be transformed to the other using the density and viscosity ratios).

Except in the limit of zero Reynolds number, the momentum equation is non-linear and generally speaking is only amenable to numerical solution. Several full numerical solutions have been published in the literature (see e.g. Juncu, 1999; Yan et al., 2002).

However, in order to gain insights into the manner in which circulation patterns might affect mass transfer (which is the focus of the present paper) it is not strictly necessary to compute the circulation pattern in complete detail: an approximation to the circulation pattern may be adequate. The key requirement for the insights we seek is that the typical speed of the circulation (measured, as far as mass transfer is concerned, via a so-called Peclet number) is matched for the approximate and true patterns. We are not claiming here that the mass transfer process is independent of the precise details of the circulation pattern–merely that similar insights into mass transfer are available from an approximate circulation pattern as from a more accurate pattern.

Approximations to circulation patterns (specifically approximations to streamline patterns) are available in the literature using drastically truncated Galerkin expansions (Uribe-Ramirez and Korchinsky, 2000a, b; Nakano and Tien, 1967). Mathematically these are (comparatively) simple functional forms defined

over the entire solution domain, which respect the same kinematic and dynamic matching conditions on the drop surface as the full circulation pattern would, and also have the correct asymptotic behaviour at long distances from the drop. They also respect the continuity equation (by construction, through being expressed in terms of a streamfunction) but satisfy the momentum equation only in some approximate (projected) sense.

Each term in the proposed Galerkin expansion contains a free coefficient, the values of which are then determined by imposing a number of boundary conditions and/or momentum equation projections equal to the number of free coefficients. The resulting coefficients become functions of the internal–external density ratio, internal–external viscosity ratio and the Reynolds number. The truncated Galerkin streamline patterns ideally have the same topology as and a similar spatial layout to those obtained by full numerical methods.

Uribe-Ramirez and Korchinsky (2000a, b) applied the Galerkin expansion to study flows for Reynolds numbers between 10 and 250. At Reynolds numbers smaller than this, the hope might be that one can (at least approximately) employ the analytical solution (Batchelor, 1967) which arises in creeping flow. Indeed the so-called Hadamard–Rybczynski streamfunction (Batchelor, 1967) is amongst the terms included in the truncated Galerkin expansion.

As Reynolds numbers increase, the true flow fields become increasingly complex. To capture properly such additional complexity, presumably requires increasing numbers of terms in a Galerkin expansion: a drastic truncation is no longer appropriate. Harrison (2006) compared velocity profiles on the drop surface (computed by the truncated Galerkin expansion) to numerical profiles published in the literature. Two different (internal) Reynolds numbers were considered, the values being 50 and 150, along with a variety of density and viscosity ratios. Agreement was fair: relative errors between the two sets of profiles were on the order of 20% provided the viscosity ratio (internal to external) was not too low (a ratio of 0.1 gave exceedingly poor agreement) and provided the density ratio (again internal to external) was not too high (again a ratio of 3 or above gave exceedingly poor agreement).

In summary the drastically truncated Galerkin expansion as used by Uribe-Ramirez and Korchinsky (2000a, b) and Harrison (2006) is believed to be a sufficiently good approximation to offer useful insights into circulating drop mass transfer, provided neither the density ratio, viscosity ratio nor the Reynolds number are too extreme. The truncated Galerkin expansion will be employed throughout this paper, specifically with the value of the Reynolds number chosen to be 30. Having decided upon a suitable flow field/circulation pattern, we now turn to consider mass transfer superposed on such a pattern.

2.3. Mass transfer in circulating drops

Mass transfer in a circulating drop (as sketched in Fig. 1) can be described via an advection–diffusion equation (Waheed et al., 2002). Even though the advection–diffusion equation is linear in solute mass fraction (at least assuming the solute diffusivities are independent of concentration, Toor, 1964a, b) analytic solution is generally not possible. The reason for this is that the velocity fields become coefficients in the mass transfer equation. The spatial variation of the velocity fields (and thereby of the above mentioned coefficients) is sufficiently complex to preclude analytic solution for the solute mass fractions. This is true even in the case where circulation patterns are given by a truncated Galerkin expansion, and indeed even in the creeping flow limit

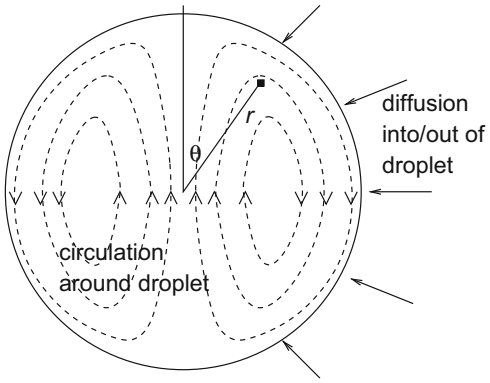

Fig. 1. Schematic of mass transfer into or out of a circulating drop. As sketched the drop is ascending, or equivalently (in the frame of the drop) the external flow is from top to bottom. An arbitrary point in the drop (■) can be specified by spherical r, θ coordinates.

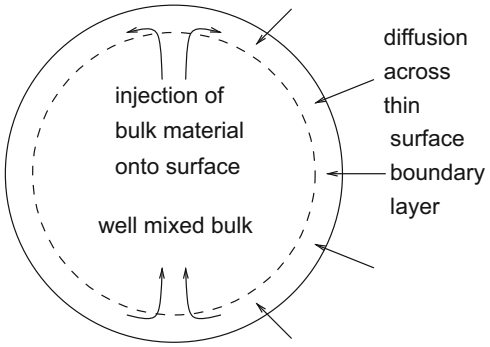

Fig. 2. Schematic of boundary layer mass transfer model.

where the analytic Hadamard–Rybczynski streamfunction can be utilised: see e.g. Juncu (2001, 2005).

One way that previous authors (Chao, 1969; Ruckenstein, 1967) have dealt with the complexity of mass transfer in circulating drops is to introduce so-called boundary layer models for mass transfer which can be tackled analytically or semi-analytically.

These boundary layer models exploit the fact that in typical circulating drops in liquid–liquid extraction, advection of mass is much faster than diffusion. Indeed Peclet numbers (see precise definition given later) of around 10 000 are not unusual. As is well established for mass transfer at high Peclet numbers (Bird et al., 1960; Leal, 2007), concentration gradients often tend to be confined to thin boundary layers.

Uribe-Ramirez and Korchinsky (2000a, b) presented a semi-analytic boundary layer theory of mass transfer in circulating drops: see Fig. 2, with full details in Appendix A. They utilised the drastically truncated Galerkin expansion approximations (Nakano and Tien, 1967) to represent the fluid flow field, and assumed that gradients of solute concentration fields occurred solely in the vicinity of the drop surface.

By and large Uribe-Ramirez and Korchinsky (2000a, b) predicted much faster equilibration of a solute concentration field with their model than was the case for a rigid drop (Negri and Korchinsky, 1986; Negri et al., 1986). Although rigid drop mass transfer permits the transient appearance of sharp concentration gradients confined to thin layers (see Section 2.1), these sharp gradients do not persist over time.

Uribe-Ramirez and Korchinsky, by contrast, applied a well-mixed assumption to their drop interior, which kept the solute

concentration gradients (in their boundary layer) sharp over time (Uribe-Ramirez and Korchinsky, 2000a, b). The mass transfer speed up which occurred in the Uribe-Ramirez and Korchinsky model (compared to the rigid drop) was dramatic: speed up was by a factor on the order of the square root of the Peclet number. For the high Peclet numbers of interest here, substantially over a 10-fold speed up was observed (as alluded to in Section 1).

One of our aims in this paper is to compare the predictions of the rigid drop model and of the Uribe-Ramirez and Korchinsky boundary layer model with full numerical simulations of the advection–diffusion equations to see which of the models agrees better with the simulations. We will find that the rigid drop model evolves more slowly compared to the numerical simulations whereas the Uribe-Ramirez and Korchinsky model evolves far more rapidly.

3. Theory and governing equations

Consider a drop of radius R, translating with respect to a surrounding liquid at speed U_{drop}. Switching to the reference frame of the drop, and provided the viscosity ratio of internal to external fluid is not too extreme, liquid at a typical point on the drop surface (e.g. on the equator) will also be circulating at a speed of the order of magnitude of U_{drop}. The time scale for a fluid element to sweep around the drop surface (and hence the time scale for fluid elements beneath the surface to execute a complete streamline orbit) will be on the order of R/U_{drop}. This represents the typical time scale of advection.

As regards diffusion, we consider typical values of diffusivity from a recent study (Korchinsky et al., 2009) on a ternary mixture of acetone–methanol–benzene (labelled components 1, 2 and 3, respectively). The scale of the diffusivities can be set by taking the average of the infinite dilution diffusivities amongst all the components. We denote this value $\langle D^0 \rangle$, and note that it depends on the system (i.e. which components are present) but not on the component concentrations. For acetone–methanol–benzene (Korchinsky et al., 2009) $\langle D^0 \rangle = 3.48 \times 10^{-9}\,\mathrm{m^2\,s^{-1}}$. Given the value of $\langle D^0 \rangle$, the typical time scale for diffusive transport is $R^2/\langle D^0 \rangle$.

The ratio between the two above mentioned time scales defines a key dimensionless group governing the advection–diffusion process in a circulating drop, namely the Peclet number Pe,

$$Pe = RU_{drop}/\langle D^0 \rangle. \tag{1}$$

For a typical drop radius R of 10^{-3} m and a typical drop velocity of U_{drop} of around $0.03\,\mathrm{m\,s^{-1}}$, it is clear that Pe is on the order of 10 000, as already stated in Section 2.3. This implies that there is a large separation of time scales between advection and diffusion: indeed in the limit of an infinite Pe, material can execute a complete streamline orbit before any diffusion has taken place.

This scale separation is the physical feature that makes simulating mass transfer in a circulating drop so challenging. We are primarily interested in long-time scale diffusive processes, but in order to access these, the simulations must resolve also the much shorter time scale advection.

In what follows, we describe the governing advection–diffusion equation (Section 3.1) with its boundary and initial conditions (Section 3.2). We also specify the fluid flow field (Section 3.3) and the various component diffusivities (Section 3.4). Moreover we show how to decouple the evolution of particular components from each other (Section 3.5).

3.1. Advection–diffusion equation

We work in a dimensionless system of units in which time is made dimensionless on the scale $R^2/\langle D^0 \rangle$, distance is made dimensionless on the scale R, and circulation velocities are made dimensionless on the scale U_{drop}. The circulation pattern is represented by a dimensionless velocity field $\boldsymbol{u}$ which is a (specified) function of dimensionless radial coordinate r and polar angle θ.

Advective–diffusive multi-component mass transfer satisfies (Bird et al., 1960)

$$\partial \boldsymbol{w}/\partial t + Pe\,\boldsymbol{u}\cdot\nabla\boldsymbol{w} = \nabla\cdot(\boldsymbol{\Delta}\nabla\boldsymbol{w}). \tag{2}$$

Here t is dimensionless time, and $\boldsymbol{w}$ is a vector of mass fractions: w_1 is the mass fraction of component 1, w_2 is the mass fraction of component 2, etc. In a ternary system (e.g. acetone–methanol–benzene as mentioned above), the vector $\boldsymbol{w}$ only contains two of the components (e.g. w_1 and w_2 say), because the sum of all mass fractions is necessarily unity. Our objective is to solve for each component mass fraction as a function of t, r and θ. The quantity $\boldsymbol{\Delta}$ is a matrix of (dimensionless) diffusivities. Specifically these are the Fickian diffusivities divided by $\langle D^0 \rangle$. The reason that $\boldsymbol{\Delta}$ is a matrix (rather than just having a single diffusivity per component) is that in a ternary (or higher) component system with more than one solute, a gradient of one solute mass fraction can induce a flux of another (Taylor and Krishna, 1993; Krishna and Wesselingh, 1997; Smith and Taylor, 1983; Krishna and Standart, 1979, 1976): thus $\boldsymbol{\Delta}$ has off-diagonal components as well as diagonal ones (although the diagonal components are generally dominant).

3.2. Boundary and initial conditions

Eq. (2) must be solved with suitable initial and boundary conditions.

Ordinarily the solution domain would include both the region internal to and that external to the drop. The initial condition would specify mass fractions inside $\boldsymbol{w}^0$ and external to $\boldsymbol{w}^0_{ext}$ the drop. The boundary conditions would be specified mass fractions in the external far field $\boldsymbol{w}^\infty_{ext}$ and a regularity condition internal to the drop at the centre. It would also be necessary to match concentrations (or more correctly chemical potentials, Taylor and Krishna, 1993) and fluxes at the drop surface: these surface concentrations and fluxes are time dependent. All the above conditions have been discussed by Uribe-Ramirez and Korchinsky (2000a, b). More generally, the drop radius may also vary gradually over time as mass transfers in or out, but this effect was ignored by Uribe-Ramirez and Korchinsky, and will also be ignored here: again recall that at the large Peclet numbers of interest, the circulation rates within the drop are inherently much faster than drop growth rates mediated by mass transfer in or out. The net mass transport rate summed over all components (1, 2 and 3 in a ternary system) depends solely on the local circulation velocity and the local density, the latter being assumed not to vary significantly spatially over the drop.

In this work, in the interests of simplicity, we shall assume that the mass fractions on the drop surface are fixed over time with specified values $\boldsymbol{w}^R$. Mathematically this assumption is convenient because it means that one only has to solve for the concentration field in the inside (say) of the drop, instead of solving a coupled mass transfer problem both inside and outside.

Fixing the surface mass fractions at $\boldsymbol{w}^R$ is an approximation which would only be justified in the limit where the mass transfer resistance inside the drop is much larger than that outside. One way of achieving this is to have a much smaller diffusivity inside

the drop than outside. However, even when the diffusivities inside and outside are comparable, it is possible to justify this approximation a posteriori on the grounds that material outside the drop sweeps past the drop surface once only, whereas that inside the drop circulates around a multitude of times. The spatial distance over which concentration gradients are set up depends on the time available to establish them. Gradients outside the drop are sharper (having limited contact time with the drop to be set up, particularly when the flow is inherently rapid, i.e. Peclet number is large) whilst those inside the drop are less sharp (indeed, contrary to what is assumed in the boundary layer model of Uribe-Ramirez and Korchinsky, 2000a, b, gradients are realised over larger distances with each successive circulation). Less sharp gradients internal to the drop imply mass transfer resistance inside the drop tends to be somewhat larger than that outside.

It is noteworthy that the opposite limit (i.e. external mass transfer resistance being dominant) has been previously considered in the literature (Juncu, 2001, 2005). However, that study was not for liquid drops suspended in another liquid, but rather for gas bubbles suspended in liquid. Diffusivities in the gas bubbles are much higher than those in the liquid, meaning external mass transfer resistance really is dominant there. In the present work, however, the focus is on liquid–liquid systems, not gas–liquid ones.

In the liquid–liquid system we shall consider here for the ternary mixture acetone–methanol–benzene (components 1, 2 and 3, respectively), we shall impose initial and boundary conditions

$$w_1^0 = 0.2, \quad w_2^0 = 0.6, \quad w_3^0 = 0.2, \tag{3}$$

$$w_1^R = 0.3, \quad w_2^R = 0.4, \quad w_3^R = 0.3. \tag{4}$$

3.3. Obtaining the flow field

We use the same flow field as Uribe-Ramirez and Korchinsky (2000a, b) (originally used by Nakano and Tien, 1967). The flow is given by a (dimensionless) streamfunction via a truncated Galerkin expansion with coefficients as follows:

$$\psi = (e_1 r^2 + e_2 r^3 + e_3 r^4)\sin^2\theta + (e_4 r^2 + e_5 r^3 + e_6 r^4)\sin^2\theta\cos\theta \tag{5}$$

from which the (dimensionless) velocity components are

$$u_r = \frac{1}{r^2 \sin\theta}\frac{\partial\psi}{\partial\theta}, \tag{6}$$

$$u_\theta = -\frac{1}{r\sin\theta}\frac{\partial\psi}{\partial r}. \tag{7}$$

Note that ψ vanishes on both the drop axis and (by suitably choosing the coefficients e_1 through e_6) the drop surface, and the sign convention is such that ψ is positive inside the drop.

The coefficients e_1, e_2, etc. depend on the drop density ratio, viscosity ratio and Reynolds number. For the purposes of this study, we shall assume unit density and viscosity ratios and a Reynolds number Re (defined here as RU_{drop}/ν, where ν is kinematic viscosity) of Re=30. For the drop envisaged above (see the discussion following Eq. (1)) with $R=10^{-3}$ m and U_{drop}= 0.03 m s^{-1}, this requires a kinematic viscosity ν on the order of 10^{-6} m^2 s^{-1}, which is a typical order of magnitude for many common solvents.[1] Under the above conditions it is then possible to show

$$e_1 = 0.390, \tag{8}$$

$$e_2 = -0.190, \tag{9}$$

$$e_3 = -0.200, \tag{10}$$

$$e_4 = 0.012, \tag{11}$$

$$e_5 = 0.288, \tag{12}$$

$$e_6 = -0.300. \tag{13}$$

Note that these coefficients are somewhat different from those that arise in the Hadamard–Rybczynski streamfunction in the creeping flow limit (Batchelor, 1967). For the same unit viscosity ratio (the density ratio now being irrelevant), it turns out e_1=0.125, e_3= −0.125 and all other coefficients vanish.

The streamline pattern associated with Eqs. (5)–(13) is plotted in Fig. 3.

3.4. Obtaining the dimensionless diffusivities

Fickian diffusivities vary with composition (Taylor and Krishna, 1993), so that $\mathbf{\Lambda}$ is in principle a function of mass fraction, making Eq. (2) non-linear in $\boldsymbol{w}$.

In most liquid–liquid extraction operations, differences in solute concentration within and between the dispersed and continuous phases are not large (Korchinsky et al., 2009). Therefore Fickian diffusivities, whilst differing from their infinite dilution counterparts, are essentially constant and uniform throughout the process. Thus $\mathbf{\Lambda}$ is effectively a constant matrix (Korchinsky et al., 2009), and Eq. (2) can be linearised (Toor, 1964a, b)

$$\frac{\partial \boldsymbol{w}}{\partial t} + Pe\,\boldsymbol{u}\cdot\nabla\boldsymbol{w} = \mathbf{\Lambda}\nabla^2\boldsymbol{w}. \tag{14}$$

Two extraction processes both working with the same system (e.g. acetone–methanol–benzene), but operating in very different composition ranges, would have different values of $\mathbf{\Lambda}$, but the value of $\mathbf{\Lambda}$ can nonetheless be assumed held constant during each individual process.

Selecting appropriate values of $\mathbf{\Lambda}$ in a given composition range requires either experimental Fickian diffusivity data in the range

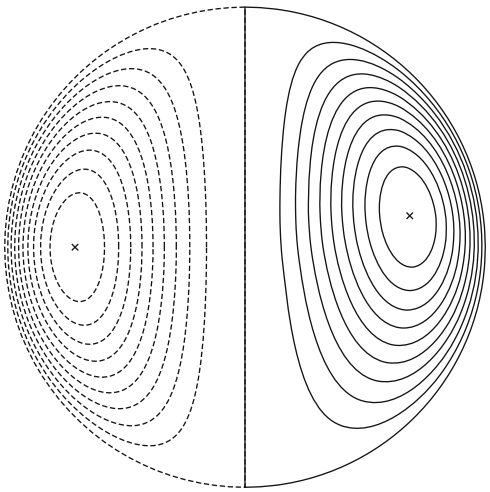

Fig. 3. Streamline pattern for the truncated Galerkin expansion (right-hand side of the figure). For comparison (left-hand side of the figure) the Hadamard–Rybczynski streamline pattern, which applies in the creeping flow limit. Equal numbers of streamlines are shown on either side, but the maximal values of the streamfunctions differ, being 0.0812 (on the right) and 0.0312 (on the left).

[1] Incidentally, for these parameter values, with a typical liquid density 1000 kg m^{-3} and a typical interfacial tension of 0.01 N m^{-1}, hydrodynamic stresses are estimated to be an order of magnitude smaller than capillary pressures, justifying, in a first approximation, an assumption of drop sphericity.

of interest or else infinite dilution diffusivity data coupled to a theory for determining diffusivities at finite compositions. Here the so-called Maxwell–Stefan theory is used (Taylor and Krishna, 1993). Further details of the method are given in a recent publication (Korchinsky et al., 2009). Briefly the method works as follows. So-called Maxwell–Stefan diffusivities are estimated at any specified composition by interpolating between infinite diffusivity data. Thermodynamic corrections to the diffusivities are then computed using activity coefficient models. Finally Fickian diffusivities are computed by combining the Maxwell–Stefan interpolations with the thermodynamic corrections.

For the ternary system acetone–methanol–benzene at composition w_1=0.25 (acetone), w_2=0.50 (methanol) and w_3=0.25 (benzene), corresponding to the midrange composition of Eqs. (3) and (4), the method (Korchinsky et al., 2009) predicts

$$\mathbf{\Delta} = \begin{pmatrix} \Delta_{11} & \Delta_{12} \\ \Delta_{21} & \Delta_{22} \end{pmatrix} = \begin{pmatrix} 0.905 & 0.112 \\ -0.041 & 0.362 \end{pmatrix}. \tag{15}$$

Note that the off-diagonal terms are smaller than the diagonal ones. Moreover Δ_{21} here is negative (which means that in the absence of an imposed gradient of component 2, the flux of component 2 is in the opposite direction to that of component 1). We shall use Eq. (15) throughout this work.

3.5. Component decoupling

Owing to the off-diagonal components of $\mathbf{\Delta}$ (Eq. (15)), the evolution of the various components of $\boldsymbol{w}$ are coupled to one another. The components of Eq. (14) can be decoupled (Toor, 1964a, b) by diagonalising the system (see also Korchinsky et al., 2009, which used this technique recently).

A matrix P and its inverse P^{-1} are sought such that

$$P^{-1}\mathbf{\Delta}P = \boldsymbol{\lambda}, \tag{16}$$

where $\boldsymbol{\lambda}$ is a diagonal matrix with elements consisting of the eigenvalues of $\mathbf{\Delta}$, the columns of P being the corresponding eigenvectors. The matrix $\boldsymbol{\lambda}$, like $\mathbf{\Delta}$, is assumed constant (i.e. independent of the composition/mass fractions) here. For the specific $\mathbf{\Delta}$ given in Eq. (15), we find

$$\boldsymbol{\lambda} = \begin{pmatrix} \lambda_1 & 0 \\ 0 & \lambda_2 \end{pmatrix} = \begin{pmatrix} 0.896 & 0 \\ 0 & 0.371 \end{pmatrix}. \tag{17}$$

Mass fractions of so-called pseudo-components are obtained by premultiplying $\boldsymbol{w}$ by P^{-1}. The analogue of Eq. (14) written in terms of pseudo-component mass fractions (denoted $\overline{\boldsymbol{w}}$) is

$$\partial\overline{\boldsymbol{w}}/\partial t + Pe\,\boldsymbol{u}\cdot\nabla\overline{\boldsymbol{w}} = \boldsymbol{\lambda}\nabla^2\overline{\boldsymbol{w}}. \tag{18}$$

The decoupled (scalar) equations (18) are solved, with initial and boundary conditions on $\overline{\boldsymbol{w}}$ (obtained by premultiplying the analogous conditions on $\boldsymbol{w}$ by P^{-1}). Finally actual component mass fractions are recovered by premultiplying the pseudo-component mass fractions by the matrix P, i.e. $\boldsymbol{w} = P\overline{\boldsymbol{w}}$.

4. Numerical methods

We solved Eq. (14) (or rather its decoupled analogue equation (18)) by two independent numerical methods, described in Sections 4.1 and 4.2. We also compared the circulating drop predictions with those of previous models: solution methods for the previous models are described in Section 4.3. The set of parametric studies that we analysed and compared is described in Section 4.4: Peclet numbers up to 1000 were simulated using the numerical method of Section 4.1, whereas Peclet numbers up to 10 000 were simulated using the method of Section 4.2.

4.1. Finite difference method

The first numerical method was a finite difference algorithm using centred spatial differences along with the alternating direction implicit method (Press et al., 1992).

Briefly the method obtains an estimate of mass fractions half way through a time step via (known) radial finite differences at the beginning of the time step and (a priori unknown) angular finite differences half way through the step. A tridiagonal matrix must then be solved to obtain the mass fractions half way through the step. Once these are obtained, the method proceeds to find mass fractions at the end of the time step. These are obtained via the average of radial finite differences at the beginning of the step (known) and at the end of the step (a priori unknown) and angular finite differences estimated half way through the step (already obtained). Another tridiagonal matrix must then be solved to obtain finally the mass fractions at the end of the step. The advantage of the alternating direction implicit method is that only relatively compact tridiagonal matrices need to be solved at each stage.

The sensitivity of the algorithm to the number of spatial finite difference points was tested by switching off the flow field i.e. setting $\boldsymbol{u} \equiv 0$, and also starting with an (artificial) initial mass fraction field which varied spatially with r and θ in the form of a spherical harmonic. Analytic (exponentially decaying) solutions to the mass transfer equations are then available (Harrison, 2006), against which convergence studies of the finite difference scheme can be performed (Harrison, 2006). For at least 64 grid intervals in both the radial and angular directions, the relative error between the analytic and finite difference solutions was less than 1%. We settled on 128 radial grid intervals and 64 angular grid intervals.

In order to test the sensitivity of the finite difference solution to the size of the numerical time step, we switched the flow field back on (and the initial condition for $\boldsymbol{w}$ was also restored to being uniform over the drop).

The permitted size of the time step can be limited both by diffusive effects and advective ones. For the Peclet numbers considered here (which are always considerably larger than unity) the limit on the time step is advectively controlled. Accordingly we used a dimensionless time step of $0.02/Pe$, which is only a small fraction of the time to execute a streamline orbit. For benchmarking purposes, we also did some runs at time step $0.002/Pe$. These only differed from the runs at $0.02/Pe$ by about 0.4% in relative terms: we decided therefore that choosing a time step of $0.02/Pe$ was sufficiently small for our predictions. This choice was supported via a formal convergence study (using a range of time steps between $0.002/Pe$ and $0.04/Pe$), enabling us to bound the error for time step $0.02/Pe$ at less than a percent in relative terms.

The algorithm was implemented in Mathcad 13, with run times on a PC between a few hours (when Pe=100) to tens of hours (when Pe=1000).

As Peclet number increased towards the regime of primary interest (Pe on the order of 10 000) run times became longer. We emphasise (see the discussion in Section 3) that this is not solely a limitation of the numerical algorithm per se, but rather a physical feature of the problem under consideration.

Moreover, on the time scale of the first circulation, a mass transfer boundary layer (Bird et al., 1960) is found to appear on the drop surface, and during this first circulation, the boundary layer achieves a (dimensionless) thickness of only $O(Pe^{-1/2})$. In order to resolve this properly, more spatial grid intervals should be used as Pe increases (e.g. 128 radial intervals may prove to be insufficient), and these should be accompanied by yet smaller time steps to regain accuracy and stability. Further restrictions on the size of grid intervals (and thereby time steps) arose from

questions of numerical stability: convective problems are generally only numerically stable provided the grid-Peclet number (defined as the drop Peclet number divided by the number of radial or angular intervals) is not too large (Heinrich et al., 1997): otherwise numerical tricks such as upwind differencing should be used (Press et al., 1992; Heinrich et al., 1997). Whilst 128 radial and 64 angular intervals proved sufficient for drop Peclet numbers $Pe=100$ and 1000, the case $Pe=10\,000$ was not stable, and would have required a finer spatial grid, and still finer time steps (or alternatively upwind differencing). The numerical challenges presented by this prompted us to explore an alternative numerical method with slightly improved computational efficiency: see Section 4.2.

4.2. Finite element method

For the largest Peclet numbers that we accessed ($Pe=10\,000$), we switched to a finite element code (Zimmerman, 2007). The commercial package Comsol Multiphysics was employed. For the flow field, the same truncated Galerkin streamline pattern as previously (i.e. Eq. (5)) was employed. Dimensionless diffusivities were given by Eq. (15) as before. Initial and boundary conditions on mass fractions were again given by Eqs. (3) and (4). The finite element code (while it does not overcome the massive separation between circulation and diffusive time scales that is inherent to large Peclet numbers) had the advantage that the computational mesh could be adjusted to have most resolution in the region where high resolution is needed (i.e. near the drop boundary), and less resolution elsewhere. Although the finite element package offers the possibility to introduce 'upwind'-type stabilisation schemes, these were not implemented here. The numerical mesh was sufficiently refined (in other words, the cell-Peclet number—being the analogue of the grid-Peclet number in Section 4.1—was kept sufficiently small), that numerical stability was not problematic, even when the drop Peclet number ranged up to 10 000.

Benchmarks were done by varying the mesh refinement between 25 800 and 220 800 degrees of freedom. As a guide, a mesh with 25 800 degrees of freedom had elements with edge lengths down to 0.004 units; a mesh with 69 300 degrees of freedom had edge lengths down to 0.002 units; meshes with 140 000, 159 300 or 220 800 degrees of freedom had edge lengths down to 0.001 units. Moreover the mesh with 159 300 degrees of freedom has 77 100 elements in total.

At $Pe=100$, the mesh with 25 800 degrees of freedom gave mass fraction predictions differing from those of the more refined meshes only at the fourth significant figure. Moreover finite element data on the more refined meshes (specifically at 159 300 degrees of freedom) were plotted against the predictions of the finite difference code for $Pe=100$ and 1000 at selected spatial points as a function of time. For $Pe=100$, finite element and finite difference data overlay one another. For $Pe=1000$, the separation between the finite element and finite difference data was comparable with the curve thickness on the plot: this corresponds to a discrepancy in only the third significant figure. All the finite element data we report in what follows is on meshes of either 140 000, 159 300 or 220 800 degrees of freedom.

Time steps were chosen adaptively by Comsol Multiphysics in the first instance. However, we also benchmarked the finite element code with respect to different maximum permitted time steps of $0.2/Pe$ vs $0.02/Pe$. Time steps were around 10^{-8} units initially, rising to the maximum permitted values as the simulation proceeded. Analogous to what was found for the finite difference code, the difference between predictions with these two different time steps occurred in the fourth significant figure. We selected $0.2/Pe$ as our maximum permitted time step. Run times on a PC were up to several hours for the largest Peclet number (i.e. $Pe=10\,000$) considered.

4.3. Comparison with predictions of previous models

Our principal aim here is to generate and analyse numerical results for mass transfer in circulating drops. However, an additional aim (alluded to in Section 2.3) is to compare the predictions of the full numerical simulations of the circulating drop to those from previous models, specifically to those of the rigid drop and of the Uribe-Ramirez and Korchinsky boundary layer model (Uribe-Ramirez and Korchinsky, 2000a, b). We give brief details of how the previous model predictions were obtained.

Analytic predictions exist for the rigid drop (Negri and Korchinsky, 1986; Negri et al., 1986). We used the separation of variables solution (see Section 2.1) with 100 Fourier series components: choosing 100 Fourier series components ensures a spatial resolution comparable with that in our finite difference code (128 radial elements). Of course the higher Fourier components decay exponentially with time exceedingly rapidly, so high spatial resolution is only essential at extremely small times.

We found that the rigid drop was about 90% of the way to equilibration after 0.3 units of dimensionless time. Since we anticipate that the circulating drop should equilibrate no slower than the rigid drop, we decided to simulate the circulating drop for 0.2 units or 0.3 units of dimensionless time.

The Uribe-Ramirez and Korchinsky (2000a, b) boundary layer model is described via an analytic or semi-analytic formula, specifically Eq. (A.18) in Appendix A, or strictly a multi-component generalisation thereof. The only numerical work needed is a quadrature over polar angle (see e.g. Eqs. (A.14) and (A.17)), and even quadrature can be dispensed with (in favour of analytic integration) in certain cases (including the one considered here).

4.4. Parametric studies

It remains to describe (and justify) the parametric studies we have done to analyse the circulating drop. We shall consider parametric runs of the circulating drop numerical simulations varying Peclet number (from $Pe=100$ to 1000 to 10 000), at fixed Reynolds number $Re=30$.

At first sight, this choice of parametric runs seems unusual. For an actual material, the Reynolds number Re varies proportional to the Peclet number: indeed the Schmidt number (defined as the ratio between Peclet and Reynolds numbers) is a material property, dependent on drop mass fractions, but independent of drop size and velocity. Experimentally one could only vary Peclet number at fixed Reynolds number, by performing experiments for an array of different materials. However, the Schmidt numbers of materials encountered in liquid–liquid extraction are almost always on the order of a few hundred (see e.g. Uribe-Ramirez and Korchinsky, 2000a). It would not be possible to find an extraction problem with Peclet number as low as $Pe=100$ (or even with $Pe=1000$) and yet simultaneously with Reynolds number as large as $Re=30$: ordinarily $Re=30$ would demand Pe on the order of 10 000. Conversely an extraction problem running at $Pe=100$ would usually have Re less than unity, and certainly not $Re=30$.

Nonetheless parametric studies varying Pe at fixed Re are useful.

There are two reasons for this. Firstly, studies at realistic values of Pe (e.g. $Pe=10\,000$) are necessarily numerically expensive for

the reason pointed out above (see Section 3): i.e. the large separation between the circulation time scale, which must be resolved, and the diffusive time scale, which generally governs mass transfer. One can consider smaller values of *Pe* which are inexpensive to simulate, and compare e.g. *Pe*=100 and 1000, so as to gain intuition about how increases in *Pe* might affect the mass transfer process.

The second reason concerns the respective influence of *Pe* and *Re* on the advective term in Eq. (14), which actually involves the product *Pe* $\boldsymbol{u}$. Here the role of *Pe* is straightforward. It governs (see Eq. (1)) the rate of orbiting streamlines relative to the rate of mass diffusion.

The role of the Reynolds number *Re* is more subtle. It appears in Eq. (14) only implicitly, due to the fact that the drop velocity field $\boldsymbol{u}$ depends on *Re* (as well as upon density and viscosity ratios). Except in cases where density and/or viscosity ratios are very extreme, $\boldsymbol{u}$ would be expected (for any given *Re*) to be a field of order unity (recall that $\boldsymbol{u}$ has already been made dimensionless with respect to U_{drop} which sets the scale of the circulation speed). Thus $\boldsymbol{u}$ governs not the circulation rate, but instead the precise spatial distribution of the velocity field (or equivalently the spatial layout of the circulation streamlines): this then is what is sensitive to Reynolds number.

After several circulations around the drop, the mass transfer field might adopt a configuration which depends on the spatial layout of the streamlines, but independent of the speed with which fluid elements circulate around those streamlines. This would imply that drop mass fractions at different Peclet numbers would asymptote (after a given number of circulations) onto a universal curve, independent of Peclet number. If and when such a configuration is reached, it would be possible to replace simulations at the actual (large) Peclet number e.g. *Pe*=10 000, with much less expensive simulations at an artificial (much smaller) value, e.g. *Pe*=1000 or even *Pe*=100. Since the mass transfer field still depends on the layout of the streamlines, it is necessary to retain the original Reynolds number (which determines that layout) even though the Peclet number has been artificially reduced.

5. Results

Here we present results of the circulating drop numerical simulations. The initial focus will be on bulk mass fractions (Section 5.1), but subsequently we consider details of local mass fractions (at selected points in the drop) vs time (Sections 5.2 and 5.3). The effect of varying Peclet number upon the results is quantified (Section 5.4). The detailed spatial layout of the mass fraction fields at selected times will also be examined (Section 5.5).

5.1. Bulk mass fraction

Bulk mass fractions are the quantities of main importance to the chemical engineer designing a liquid–liquid extraction column. Of primary interest is the total mass of the various components transferred into or out of the drop: details of the precise spatiotemporal distribution of the solute concentration field (whilst still interesting and useful to know) are less crucial. Moreover bulk mass fractions are much easier to measure experimentally than spatiotemporal variations in the solute concentration field.

Figs. 4 and 5 show bulk mass fractions vs time, respectively, for component 1 and component 2. Note the logarithmic scale for time. Circulating drop numerical simulations are shown for three Peclet numbers *Pe*=100, 1000 and 10 000; the Reynolds number is

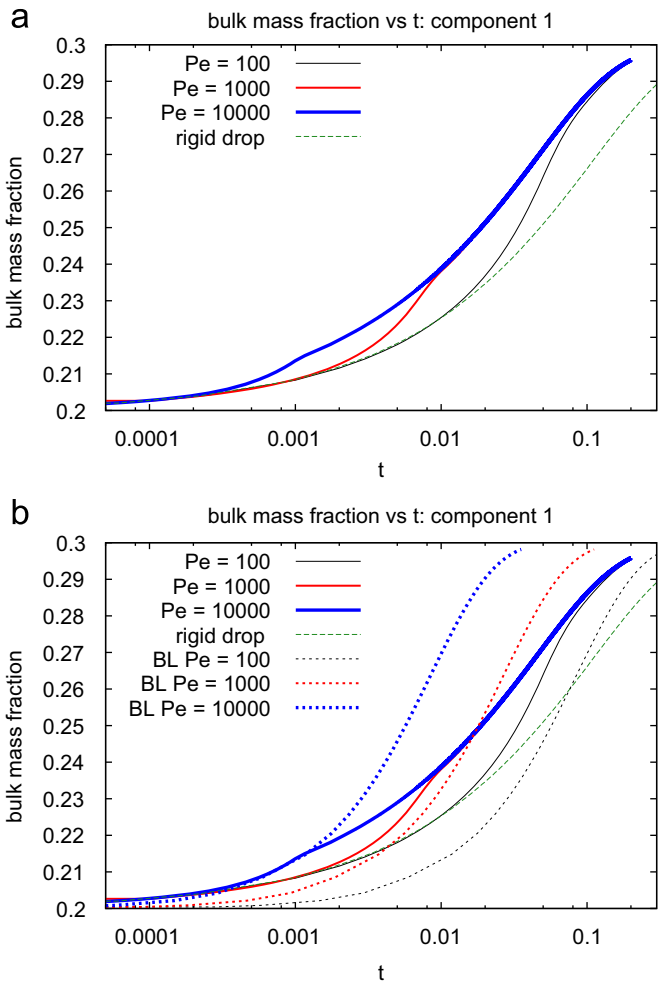

Fig. 4. Bulk mass fraction data for component 1 predicted (a) from full numerical simulations of the circulating drop, and compared to predictions of the rigid drop model and (b) to predictions of the Uribe-Ramirez and Korchinsky boundary layer (BL) model.

Re=30 throughout. Computations for the rigid drop model and the boundary layer model are also shown.

5.1.1. Comparison between circulating drop and rigid drop predictions

Clearly the circulating drop simulations (at all three Peclet numbers considered) and the rigid drop simulations all coincide at sufficiently early times: before the circulation has led to any significant turnover of the fluid at or near the surface, the system behaves as a rigid drop. However, at a (dimensionless) time of around 2/*Pe* (for each *Pe*), the circulating drop simulations start to deviate from the rigid drop predictions: the presence of the circulation leads to a faster evolution of mass fraction. Around a time of 10/*Pe* (again for each *Pe*) all the circulating drop simulations appear to come together onto a master curve: predictions are then independent of the Peclet number. At some time *t* beyond this point, one could (without significant loss of accuracy) artificially change the Peclet number to a lower value, providing that the new lower Peclet number is at least 10/*t*, ensuring that its data have likewise joined the master curve. This then permits a larger time step in the simulations and thereby faster simulations overall. A coarser mesh could then also be utilised, further reducing the computational cost. Note that the Peclet-number-independent master curve is quite distinct from the rigid drop predictions. It can be shown that by dimensionless

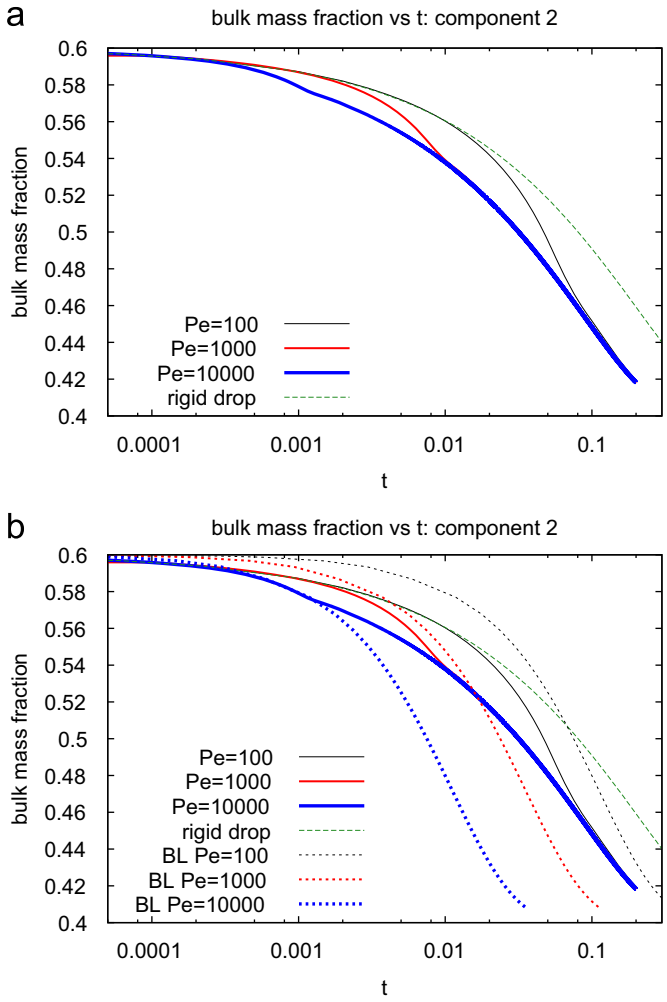

Fig. 5. Bulk mass fraction data for component 2 predicted (a) from full numerical simulations of the circulating drop, and compared to predictions of the rigid drop model and (b) to predictions of the Uribe-Ramirez and Korchinsky boundary layer (BL) model.

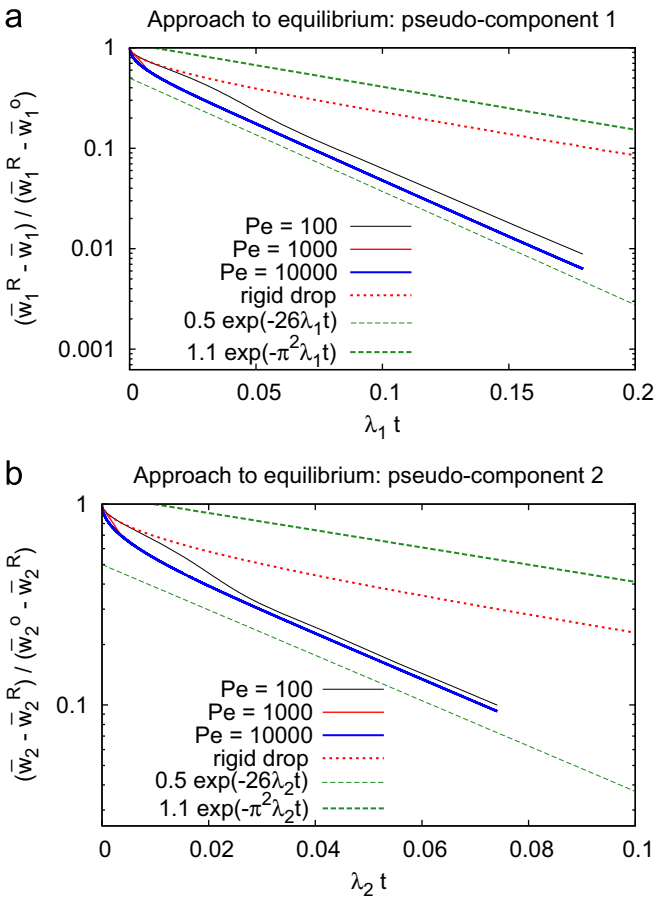

Fig. 6. Circulating drop ratios of pseudo-mass fractions (a) $(\overline{w}_1^R-\overline{w}_1)/(\overline{w}_1^R-\overline{w}_1^0)$ and (b) $(\overline{w}_2-\overline{w}_2^R)/(\overline{w}_2^0-\overline{w}_2^R)$ on the approach to the equilibrium, plotted against time. Here we plot data for pseudo-mass fractions (which evolve independently of one another) instead of mass fractions (which are coupled). The functions $0.5\exp(-26\lambda_1 t)$ and $0.5\exp(-26\lambda_2 t)$ demonstrate that the final rates of approach to equilibrium are, respectively, $26\lambda_1$ and $26\lambda_2$ for the circulating drop data: the multiplicative prefactor 0.5 here is arbitrary (and is selected to offset the plotted function slightly from the circulating drop data to aid clarity). Data for the rigid drop are also shown, with the functions $1.1\exp(-\pi^2\lambda_1 t)$ and $1.1\exp(-\pi^2\lambda_2 t)$ demonstrating the final rates of approach, $\pi^2\lambda_1$ and $\pi^2\lambda_2$. Again the multiplicative prefactor 1.1 here is arbitrary, offsetting the plotted function from the rigid drop data for clarity.

time t of around 0.03 the simulated circulating drop bulk mass fractions on the master curve are already half way to equilibrium, whereas the rigid drop needs a time of around 0.08 to achieve the same bulk mass fractions. By dimensionless time t of around 0.2, the master curve has very nearly equilibrated, whereas (at time 0.3) the rigid drop evolution is still some detectable amount away from equilibrium.

It is possible to quantify the speed up of mass transfer in the circulating drop compared to the rigid drop by looking at the final rate of approach to steady state in both cases. We consider (decoupled) pseudo-component mass fractions (see Section 3.5), instead of actual component mass fractions (which are coupled). Using a Fourier analysis (Negri and Korchinsky, 1986; Korchinsky et al., 2009), the rigid drop mass fractions approach their equilibrium state exponentially with a (dimensionless) rate constant $\pi^2\boldsymbol{\lambda}$, where $\boldsymbol{\lambda}$ is the diagonal matrix of eigenvalues of the dimensionless diffusivity $\boldsymbol{\Lambda}$ matrix (see Eq. (17)). Numerically we find the circulating drop approaches its final equilibrium state exponentially with a (fitted) rate constant 26 λ: see Fig. 6. This corresponds to nearly a threefold speed up in equilibration rate for the circulating drop compared to the rigid drop.

Fig. 6 shows a very close correspondence between $Pe=1000$ and 10 000 data (after a brief initial transient), but it also reveals a slight offset between the $Pe=100$ data and the data at higher Pe. Despite the offset, the $Pe=100$ data are still relatively close to the higher Pe data (compared to how much they differ from the rigid drop case). The $Pe=100$ offset is also substantially smaller for pseudo-component 2 than for pseudo-component 1: this is unsurprising, since in Eq. (17), pseudo-component 2 has the smaller eigenvalue—diffusion is inherently weaker for pseudo-component 2 (compared to pseudo-component 1) and so, in relative terms, convective effects are stronger. The slightly larger offset for pseudo-component 1 does not preclude $Pe=100$ data for actual components joining onto a master curve. Indeed by the time $t\approx 0.1$ at which the $Pe=100$ data in Figs. 4 and 5 appear to join a master curve, it turns out that $\overline{w}_1^R-\overline{w}_1$ is already negligibly small compared to $\overline{w}_2-\overline{w}_2^R$, meaning the values of $w_1^R-w_1$ and $w_2-w_2^R$ are both dominated by contributions from pseudo-component 2.

5.1.2. Comparison with predictions of the boundary layer model

Also shown in Figs. 4 and 5 are predictions of the Uribe-Ramirez and Korchinsky boundary layer model, at the three Peclet numbers in question ($Pe=100$, 1000 and 10 000). Note that the predictions at different Peclet numbers are all essentially the

same curve just with the time axis rescaled: t always appears multiplied by $\sqrt{Pe}$ in the Uribe-Ramirez and Korchinsky formula (the formula is essentially a multi-component analogue of single component Eq. (A.18)).

First we compare predictions of the boundary layer model with the rigid drop.

Somewhat surprisingly the Pe=100 boundary layer model is predicted to change more slowly than the rigid drop for much of its evolution, although its final approach to equilibrium is faster. The Pe=1000 and 10 000 cases also appear to evolve more slowly than the rigid drop at very early times, but this accounts for only an extremely small fraction of the overall evolution, and the final approach to equilibrium is much faster. The slow evolution at early times is a consequence of the particular way Uribe-Ramirez and Korchinsky idealised the boundary layer model. They assumed a steady state boundary layer thickness at all times; strictly speaking (see Appendix A) the model should allow the boundary layer to start very thin and grow toward steady state. With that modification (not implemented here), the boundary layer model should always evolve at least as rapidly as the rigid drop. The boundary layer should achieve its steady state thickness increasingly rapidly as Peclet number grows, which is why the Pe=100 case appears to evolve more slowly than the rigid drop for a substantial period of time, whereas the Pe=1000 and 10 000 cases only do so very briefly. Moreover the steady state boundary layer thickness increases as Pe decreases, and so overestimates the true (time-dependent) layer thickness to a greater extent at low Pe: the evolution rate of the bulk mass fraction is thereby underestimated to a greater extent (as well as for a more substantial period of time) at low Pe. To summarise, the apparent slow initial evolution of the boundary layer model compared to the rigid drop is not an inherent feature of the boundary layer model, but rather an artifact of the way in which Uribe-Ramirez and Korchinsky idealised it: this artifact becomes less significant as Pe grows.

As was noted above, the final approach of the mass fractions to equilibrium predicted by the boundary layer model (with Pe=100) is faster than what is predicted for a rigid drop, but the difference is not dramatic. Mathematically mass fractions computed via the boundary layer model have (see Appendix A) an exponential approach to equilibrium with a (dimensionless) rate constant $1.50\,Pe^{1/2}\boldsymbol{\lambda}^{1/2}$. The factor 1.50 depends on the set of Galerkin coefficients used to describe the flow field (and is the value corresponding to the coefficients given in Eq. (8)–(13)), and $\boldsymbol{\lambda}$ is (as above) the diagonal matrix of eigenvalues of the dimensionless diffusivity. Meanwhile, as mentioned previously, the rigid drop model has a final exponential approach to equilibrium with a (dimensionless) rate constant $\pi^2\boldsymbol{\lambda}$ (corresponding to the slowest decaying Fourier mode, Negri and Korchinsky, 1986; Korchinsky et al., 2009), and there are even faster decaying modes present earlier on. Comparing these two rate constants, clearly the boundary layer model (assuming a layer of steady thickness) only equilibrates significantly faster than the rigid drop if Pe is greater than about 100 (assuming the eigenvalues in $\boldsymbol{\lambda}$ are near unity). Indeed it is only meaningful to consider a boundary layer model when the boundary layer is sufficiently thin (i.e. significantly thinner than the radius of the drop), and this typically requires Pe to be around 100 or higher. Moreover when we increase Pe up to 1000 or 10 000, the final approach to equilibrium of the boundary layer model becomes substantially higher than that of the rigid drop as Figs. 4 and 5 clearly show.

Comparing now the boundary layer predictions and the full numerical simulations of the circulating drop, it so happens that the predictions of the boundary layer model with Pe=100 and 1000 straddle the Pe-independent master curve for the full numerical simulations. However, this is mere coincidence as the equilibration times in the different models scale differently: the boundary layer model equilibrates in $O(Pe^{-1/2})$ units of dimensionless time, whereas the full numerical simulations equilibrate in $O(1)$ units of time.

Indeed the most appropriate comparison to make is between the Pe=10 000 boundary layer model and the full numerical simulations: from Section 3, Pe=10 000 is a realistic value for Peclet number (given Reynolds number Re=30).

If we assume Pe=10 000 and also specific $\boldsymbol{\lambda}$ values from Eq. (17), we can compare the rate constants for approach to equilibrium of pseudo-component mass fractions in the boundary layer model ($1.50\,Pe^{1/2}\boldsymbol{\lambda}^{1/2}$) and the full numerical simulations ($26\,\boldsymbol{\lambda}$; see Section 5.1.1). The boundary layer model predicts 6 times speed up for one pseudo-component and 9 times speed up for the other. Hence, as the Peclet number increases towards the regime of physical interest (on the order of tens of thousands), the boundary layer model evolves more rapidly than the circulating drop numerical simulations, by (in order of magnitude terms) a factor of approximately 10. The substantially rapid approach to equilibrium of the boundary layer model is thereby highlighted.

The explanation for the boundary layer model's more rapid evolution is that fluid elements are assumed to be well mixed in the interior of the drop. Fluid elements which pass near the drop surface, subsequently travel through the interior, and then are re-injected onto the drop surface, are assumed to arrive at the surface ready to transfer yet more mass. Good mixing is likely to occur in a turbulent drop (and a boundary layer model may work very well under such circumstances), but here (see Section 3.3) we assume a laminar flow field at Reynolds number Re=30. If good mixing does not occur, then fluid elements which passed initially near the drop surface (and transferred mass at that time) would not gain or lose much mass upon being re-injected (since they would already be at mass fractions similar to those imposed on the surface). In order to investigate whether or not there is good 'mixing' (i.e. efficient mass transfer) in the drop interior, we consider (in the next subsection) mass fractions vs time at various points along the drop axis: on-axis data are relevant because the same fluid streamlines which pass close to the drop surface (and exchange mass there), also pass along the drop axis.

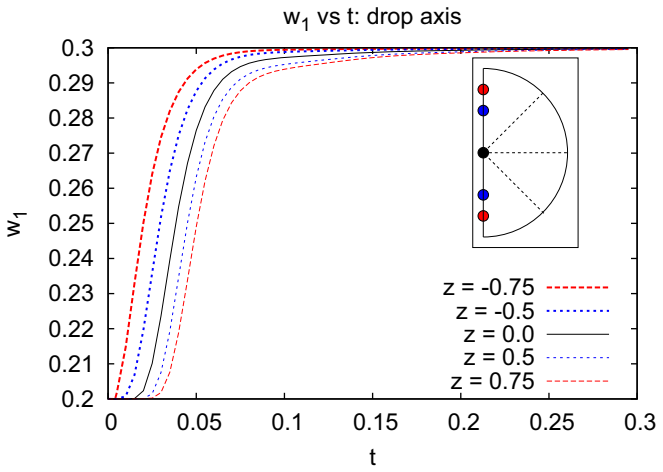

Fig. 7. Data for component 1 mass fraction vs time on the drop axis at various heights $z \equiv r\cos\theta$ with θ equal to either 0 or π. The Peclet number is Pe=100. The inset indicates on a sketch of the drop, the spatial location of the points for which data are plotted.

5.2. Mass fraction vs time: on the drop axis

Fig. 7 shows mass fraction data for component 1 at various heights on the drop axis (the height is $z \equiv r\cos\theta$ with θ either 0 or π) for $Pe=100$. Here (see also the definition sketch in Fig. 1) the location $r=1$, $\theta=0$ (and hence $z=1$) corresponds to the forward stagnation point, whereas $r=1$, $\theta=\pi$ (and hence $z=-1$) corresponds to the rear stagnation point.

It is clear that at quite early times (i.e. at times much smaller than those at which the bulk mass fraction equilibrates) w_1 migrates from values close to w_1^0 to values near w_1^R, e.g. the centre of the drop undergoes the transition from w_1^0 to w_1^R in the interval between times $t=0.02$ and 0.06 (i.e. between $2/Pe$ and $6/Pe$). This transition corresponds to fluid elements gaining mass through close contact with the drop surface, and then being advected along the drop axis *without* exchanging much mass axially (and moreover with diffusion in the direction normal to the drop axis being quite limited). This also explains why, in Fig. 7, points on the axis below (above) the equator undergo their transition sooner (later) than the drop centre does, since fluid elements from near the surface reach those points sooner (later). Although we do not present any data here for component 2 (only for component 1), we have found that component 2 shows analogous behaviour: i.e. a transition from w_2^0 to w_2^R for each point on the drop axis with little mass transfer in the drop interior.

There are good reasons to expect comparatively little mass transfer as fluid elements travel up the drop axis in a steady laminar flow. Consider first a fluid element migrating along the drop surface, which is known to be exposed to the surface for a (dimensionless) time $O(1/Pe)$. During this time, a mass transfer boundary layer transverse to the surface can grow to a thickness $O(Pe^{-1/2})$, the mass fractions changing spatially from $\boldsymbol{w}^R$ to $\boldsymbol{w}^0$ across this layer. However, streamlines which are a typical distance $O(Pe^{-1/2})$ from the drop *surface* form (on geometric grounds) a streamtube along the *axis* of thickness $O(Pe^{-1/4})$ which is considerably larger than $O(Pe^{-1/2})$ (indeed Fig. 3 gives an indication of the degree to which streamlines spread out near the drop axis).

In this axial streamtube, the diffusive term $\Delta\nabla^2\boldsymbol{w}$ in Eq. (14) has an estimated magnitude $O(Pe^{1/2}(\boldsymbol{w}^R-\boldsymbol{w}^0))$. This equals the Lagrangian derivative of the mass fraction $\mathrm{D}\boldsymbol{w}/\mathrm{D}t$. Since fluid elements take time $O(1/Pe)$ to migrate up the drop axis (from rear to forward stagnation point), at most they change their mass fraction by $O(Pe^{-1/2}(\boldsymbol{w}^R-\boldsymbol{w}^0))$: as Pe is considerably larger than unity, this represents inefficient mass transfer. Mass exchange is predicted to be suppressed as fluid elements travel up the drop axis, and is only reactivated as streamline orbits carry elements away from the axis again.

5.2.1. Mass fraction following fluid elements up the drop axis

The argument just presented suggests comparatively little diffusive mass transfer to or from fluid elements during their transit along the drop axis: we now examine the extent to which the simulation data support this. Fig. 8 shows data at three locations on the drop axis $z=-0.75$ (below the centre), $z=0$ (the drop centre) and $z=0.75$ (above the centre). Instead of the current time t, we choose the abscissa to be a quantity t_c, defined as the time at which a fluid element at any of the three locations passes the drop centre. Clearly for the drop centre, $t_c=t$. Meanwhile for $z=-0.75$, $t_c>t$, since the fluid element only reaches the drop centre after the current time t. Likewise for $z=0.75$, $t_c<t$, since the fluid element has already passed through the drop centre prior to time t. Thus t_c labels fluid elements. The ordinate is the value of w_1 at whatever time the fluid element needs to pass

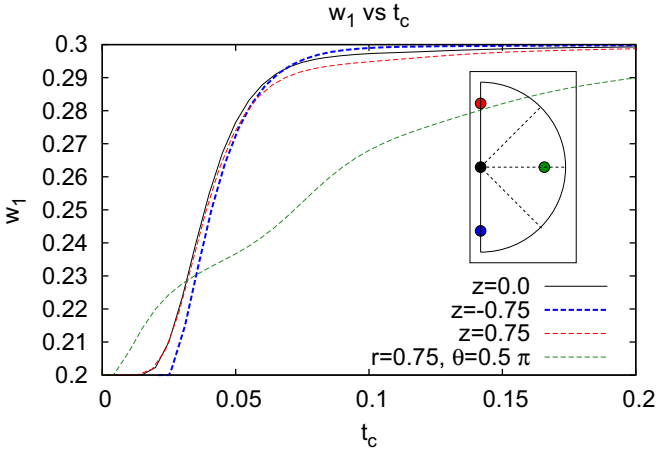

Fig. 8. Mass fractions w_1 of fluid elements on the drop axis (at positions $z=-0.75$, 0 and 0.75) vs the time t_c at which the given fluid element reaches the drop centre. The Peclet number is $Pe=100$. Data (w_1 vs t) on the equatorial plane ($\theta=\pi/2$, $r=0.75$) are also shown for comparison. The inset indicates the spatial locations for which data are plotted.

the location in question ($z=-0.75$, 0 or 0.75), so as to ensure that the element is at the drop centre at time t_c.

In this case $Pe=100$, for t_c values up to nearly 0.05 (i.e. $5/Pe$), it is clear that, on the upper part of the drop axis, while different fluid elements have different w_1 values, there is virtually no change in mass fraction following an element: the w_1 vs t_c plots for $z=0$ and 0.75 virtually overlie one another.

The picture along the lower drop axis is rather different. Somewhat surprisingly, the w_1 vs t_c curve for $z=-0.75$ underlies those for $z=0$ and 0.75. Instead of the mass fraction w_1 being high on the drop axis, and fluid elements thereby losing small amounts of mass diffusively normal to the axis, w_1 following a fluid element, actually *grows* as the element moves. At $Pe=100$, streamwise diffusion starting from the drop surface (in the neighbourhood of the rear stagnation point) can extend along the axis all the way to $z=-0.75$, and so a fluid element at $z=-0.75$ is still *gaining* mass diffusively.

Still for the case $Pe=100$, beyond t_c values of about 0.1 (i.e. $10/Pe$), the curves start to level off. It is clear at this point that the value of w_1 for a fluid element passing $z=-0.75$ is slightly higher than when the same fluid element passes the drop centre, which is slightly higher again than when the same fluid element passes $z=0.75$. Individual fluid elements therefore lose a small amount of mass during their transit up the axis, this mass being lost by diffusion normal to the axis. However, the net change in mass fraction for these fluid elements is insignificant compared to the spatial differences in mass fraction which still persist between different parts of the drop. The figure shows (for comparison) the state of an element at $r=0.75$ on the equatorial plane, which has altogether a very different w_1 value.

5.3. Mass fraction vs time: equatorial plane

The previous subsection treated mass fractions at points along the drop axis: on-axis mass fractions tended to evolve on an advective time scale ($O(1/Pe)$ dimensionless units). Here we consider the evolution of mass fractions at points on the drop equatorial plane: we will see that, in many cases, evolution is on a diffusive time scale ($O(1)$ dimensionless units). As in Section 5.2, the focus is upon component 1, the results for component 2 being broadly analogous.

Fig. 9 shows data for mass fraction w_1 vs time on the equatorial plane for radii $r=0$ (the drop centre), $r=0.25$, 0.5, 0.75 and 0.992 for $Pe=100$. Data for $r=0.992$ equilibrate very rapidly indeed,

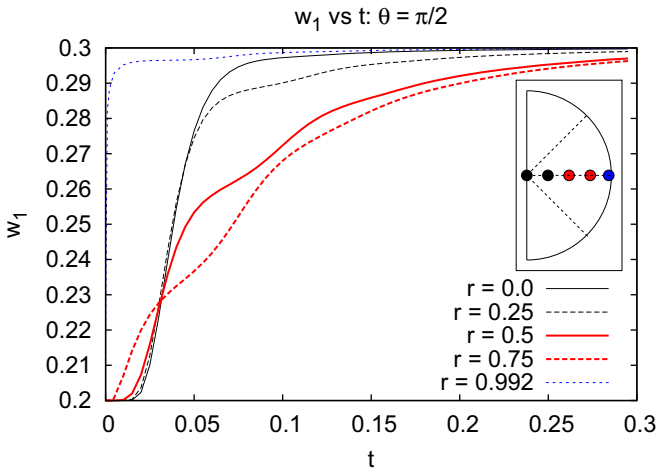

Fig. 9. Data for component 1 mass fraction vs time in the equatorial plane $\theta=\pi/2$ at various radial positions r=0, 0.25, 0.5, 0.75 and 0.992. The Peclet number is Pe=100. The inset indicates the spatial locations for which data are plotted.

whilst r=0.75 shows the next most rapid (initial) growth, with r=0.5 the next most rapid after that. However, the (initial) growth rate for r=0.75 is considerably less than that for r=0.992, and that for r=0.5 is considerably less again than what is seen for r=0.75. These initial growths are diffusive in origin, and this is why the mass fraction at the points nearer the surface grows faster.

For times greater than about 0.02 (i.e. greater than $2/Pe$ in this Pe=100 case) the mass fractions nearer the drop centre (i.e. r=0 and 0.25) begin to increase suddenly and overtake (by $t=3/Pe$) those at r=0.5 and 0.75. Indeed by $t=5/Pe$, mass fractions at r=0 and 0.25 are already 70–80% of the way to equilibrium. As has been discussed in Section 5.2, this corresponds to material from extremely close to the surface, travelling into the drop interior and up the drop axis: remember that any material in a surface boundary layer of thickness $O(Pe^{-1/2})$, forms a streamtube of thickness $O(Pe^{-1/4})$. At the modest Peclet number Pe=100 in Fig. 9, it is unlikely that this streamtube will be exceedingly thin. Indeed given the close agreement between the mass fractions at r=0 and 0.25 in Fig. 9, it would appear that for Pe=100 the streamtube extends out to at least r=0.25.

Compared to the sudden increase in mass fractions at r=0 and 0.25 noted above, mass fractions at r=0.5 and 0.75 evolve comparatively slowly over longer times. This evolution is consistent with mass fractions being fairly uniform along any given streamline (see also Section 5.5 later), but being transported slowly (i.e. diffusively) from one streamline to another: by definition there is no advection in the cross-stream direction. In this cross-stream diffusion picture (see Appendix B), the slowest evolution of all is expected for the internal stagnation point (see Fig. 10). For the streamfunction described by Eq. (5) with coefficients in Eqs. (8)–(13), the internal stagnation point (see also Fig. 3) turns out to be at $r\approx0.698$ and $\theta\approx1.38$ (i.e. quite close to the equatorial plane). Thus the points r=0.5 and 0.75 on the equatorial plane effectively straddle the internal stagnation point: their evolution will be slightly more rapid than that of the internal stagnation point, but certainly less rapid than that of points at r=0 and 0.25 which benefit from advective transport from the surface to the axis (and its neighbourhood).

5.3.1. Oscillations superposed on the mass transfer rate

In Fig. 9 the mass transfer rate is seen to fluctuate over time: at a given r value, oscillations are superposed on the general growth of w_1. The time scale of these oscillations correlates with the characteristic advection time $O(1/Pe)$.

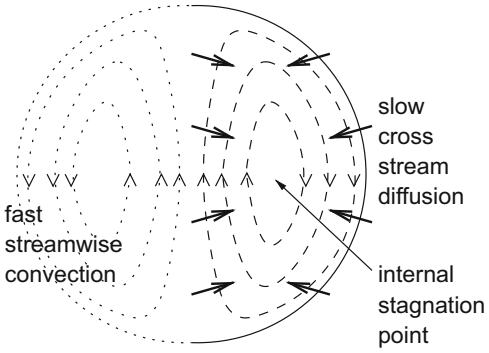

Fig. 10. Schematic of a cross-stream diffusion picture of mass transfer, with mass being transported from the drop surface and axis towards the internal stagnation point.

This makes physical sense: consider an arbitrarily chosen point e.g. r=0.75, $\theta=\pi/2$ in Fig. 9. During the first streamline orbit, some mass reaches this point diffusively, and so the mass fraction of w_1 will grow, as fluid elements have more and more time to exchange mass. However, there will come a time when fluid elements arriving at this chosen point originated from locations deep in the drop interior. All fluid elements originating deep in the interior are at present essentially equivalent as far as their w_1 goes: the only opportunity they have for exchanging mass is the period of time since they left the deep interior. Thus the growth of w_1 at the chosen point r=0.75, $\theta=\pi/2$ is temporarily arrested. Only when the first streamline orbit is more advanced, so that fluid elements have been previously at larger r values (near to r=0.75), have penetrated the deep interior and returned to larger r values, can w_1 begin to grow again.

To summarise, the exact growth rate of w_1 at any given point in space and time depends on the details of the local concentration field: the local concentration gradients (which determine this growth rate) depend on the history of a fluid element and its neighbours. Different streamlines (corresponding to different r values in Fig. 9) have different orbit times, meaning that fluid elements on adjacent streamlines circulate at different rates. Therefore mass exchange between fluid elements on adjacent streamlines is complex. Owing to the differential circulation rates, initially adjacent fluid elements on adjacent streamlines will lose contact, and be replaced by new neighbouring elements. Over time (i.e. after a few streamline orbits) a fluid element will have seen a succession of many neighbours, and will experience only an average of the state of its adjacent streamlines: oscillations are then expected to disappear (as indeed is seen in Fig. 9). Moreover the bulk mass fraction (which is an average of the mass fractions both along and across many streamlines) smooths out the oscillatory behaviour: hence no oscillations are seen in Fig. 4 for instance.

5.4. Comparing Pe=100 and 1000 data

In this subsection we consider data for Pe=1000 and compare them against Pe=100 data in the previous Sections 5.2 and 5.3. Again the focus is on component 1, with component 2 behaving analogously.

Physically we expect an increase in Pe to raise the importance of advection relative to diffusion, and this is exactly what we shall see. Remember (see Sections 2.3 and 3) that the problems of physical interest (at least those with Reynolds number Re=30 as we assume) actually have Pe in the range of tens of thousands. However, simulations at Pe=100 and 1000 are numerically cheaper, and comparing these two different Peclet numbers gives

us sufficient insight into what will happen as Peclet number is further increased (see Section 4.4). What we find by comparing the cases $Pe=100$ and 1000 is similar to what we would learn by comparing the cases $Pe=1000$ and 10 000: hence data for $Pe=10\,000$ are not specifically considered here.

5.4.1. Comparison on the drop axis

Data for w_1 vs t at selected points on the drop axis for $Pe=1000$ turn out to be qualitatively similar to those for $Pe=100$ (which are shown in Fig. 7): increases in mass fraction with time at each location are associated with advection up the drop axis. Quantitatively, however, the $Pe=1000$ data evolve on a time scale 10 times shorter than that for $Pe=100$: this reflects a nominal 10-fold speed up in the advection rate from $Pe=100$ to 1000.

Fig. 11 shows on axis data for $Pe=1000$ at heights $z=\pm 0.75$ as well as at the drop centre. As in Fig. 8, the abscissa is now t_c (the time at which a given fluid element passes the drop centre) rather than the current time t.

At $Pe=1000$, for all intents and purposes, the w_1 vs t_c curves (at different z values) overlie one another up to $t_c=10/Pe$. The asymptotic arguments presented in Section 5.2, explaining why fluid elements transfer comparatively little mass as they migrate up the drop axis, certainly appear valid here. The curves in Fig. 11 at different z values overlie one another, not only for $z=0$ and 0.75 (as occurred for Fig. 8), but also for $z=-0.75$ (contrast Fig. 8). In Fig. 11, diffusion is much weaker at this higher Peclet number $Pe=1000$, so there is no longer any possibility of a fluid element at $z=-0.75$ still growing its mass fraction via diffusion in from the surface.

Beyond t_c values of $10/Pe$, again (as was also seen in Fig. 8) the curves level off, and once again w_1 decreases very slightly from $z=-0.75$ to 0 and again from $z=0$ to 0.75. However, this slight difference in mass fraction following a fluid element up the axis is insignificant (it scales as $O(Pe^{-1/2})$ via the arguments of Section 5.2): any fluid element on the axis is near to equilibrium, whereas elsewhere in the drop (e.g. at $r=0.75$ on the equatorial plane which is shown in Fig. 11) w_1 has barely changed from the initial value.

5.4.2. Comparison on the drop equatorial plane

We turn now from the drop axis to the equatorial plane. Fig. 12 shows $Pe=1000$ data on the equatorial plane at various radial positions. Here the scale of the time coordinate is the same as in Fig. 9 for $Pe=100$: there is no speed up of the approach to

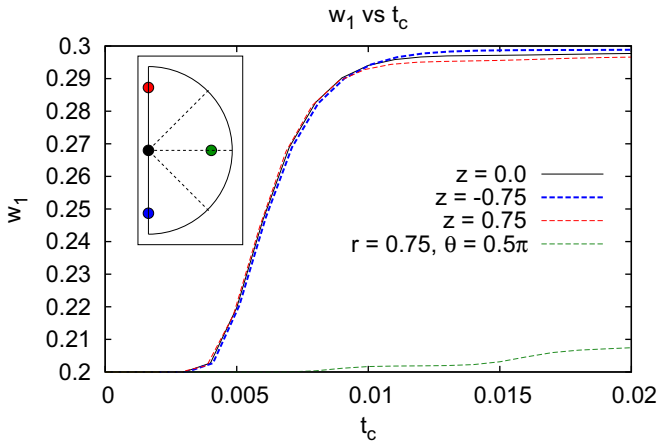

Fig. 11. Mass fractions w_1 of fluid elements on the drop axis (at positions $z=-0.75$, 0 and 0.75) vs the time t_c at which the given fluid element reaches the drop centre. The Peclet number is $Pe=1000$. Data (w_1 vs t) on the equatorial plane ($\theta=\pi/2$, $r=0.75$) are also shown for comparison.

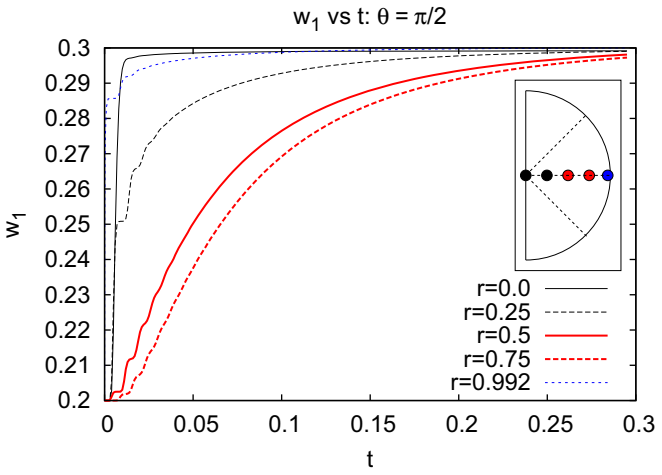

Fig. 12. Data for component 1 mass fraction vs time in the equatorial plane $\theta=\pi/2$ at various radial positions $r=0$, 0.25, 0.5, 0.75 and 0.992. The Peclet number is $Pe=1000$.

equilibrium by a factor of 10, and for the most part (i.e. for most radial positions), the ultimate rate of achieving equilibrium is diffusively controlled, depending on diffusion across fluid streamlines.

Changing the advection rate by a factor of 10 affects, however, the oscillations superposed on the general diffusive growth of w_1. The oscillation time scale correlates with streamline orbit times: higher frequency oscillations are therefore seen in Fig. 12 than in Fig. 9 (orbit times scale as $O(1/Pe)$ in our units).

At early times (i.e. well before equilibrium is attained) we can see the effect of advection being strengthened as Pe increases. In Fig. 9, the initial (diffusive) growth of w_1 at $r=0.75$ and 0.5 managed to exceed the growth of $r=0$ and 0.25 (which only exhibit growth once material is advected from the drop surface into the drop centre). In Fig. 12 by contrast, the growth at $r=0$ and 0.25 (due to advection) occurs much earlier, at times well before any significant diffusive growth has occurred at $r=0.75$ and 0.5.

5.5. Contour plots for mass fraction

Sections 5.2–5.4 all considered details of mass fraction at fixed spatial locations as a function of time. It is also instructive to consider mass fraction at fixed values of time as a function of spatial location. Here we present these data in the form of contour plots of mass fraction w_1. Again (as in Section 5.4) we consider the particular cases $Pe=100$ and 1000. Data for $Pe=10\,000$ are not shown here, since the comparison between $Pe=100$ and 1000 is adequate to reveal the trends that occur upon increasing Peclet number.

5.5.1. Contour plots for Pe=100

Fig. 13 shows contour plots for w_1 for $Pe=100$ and times $t=0.01$, 0.02, 0.05 and 0.1. Streamlines (see also Fig. 3) are superposed on the plots, allowing us to determine (for each value of time) whether (or not) contours of the mass fraction match those of the streamfunction, which is a signature of mass fraction being uniform along streamlines.

At time $t=0.01$ (i.e. $t=1/Pe$) gradients of mass fraction are confined near the drop surface, and are primarily radial: see Fig. 13(a). Mass fraction therefore varies quite substantially along streamlines. It is also easy to see that gradients tend to be sharper near the forward stagnation point than near the rear stagnation point. The reason is that advection is towards the drop surface (competing with diffusion) at the forward stagnation point, and

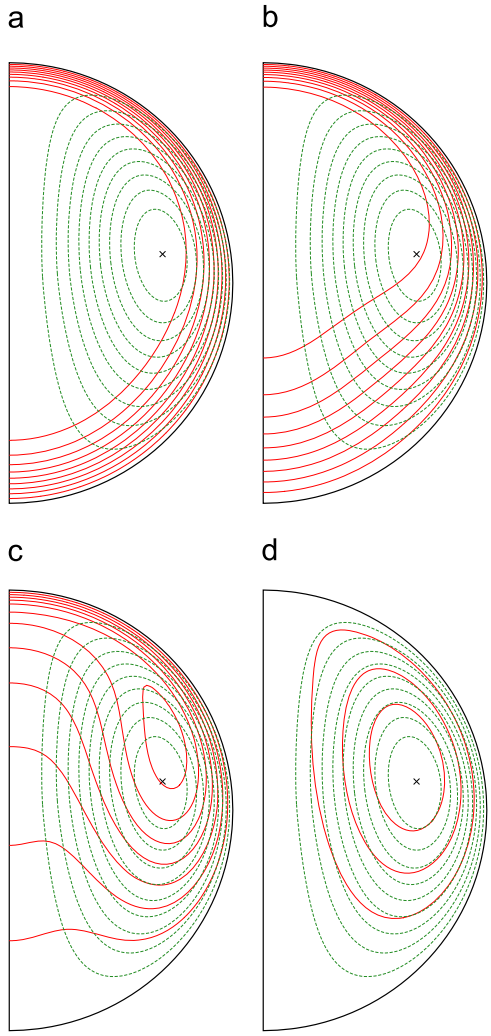

Fig. 13. Contours of mass fraction w_1 for $Pe=100$ at times (a) $t=0.01$, (b) $t=0.02$, (c) $t=0.05$, and (d) $t=0.1$. The drop surface has $w_1=0.3$ always, and the remaining contours have $w_1=0.29$, 0.28, 0.27, etc. Plots at later times have fewer contours because w_1 does not extend all the way down to the initial value 0.2: specifically the w_1 values at the internal stagnation point—which exhibits the slowest evolution—are (a) 0.201, (b) 0.208, (c) 0.230, and (d) 0.262. The streamline pattern is superposed on each plot.

away from it (cooperating with diffusion) at the rear stagnation point, which is also in line with predictions of an approximate analytical solution for the concentration field (Bird et al., 1960) (which applies locally in the neighbourhoods of the forward and rear stagnation points, and for times up to one typical streamline orbit).

At time $t=0.02$ (i.e. $2/Pe$) gradients are still primarily radial, but penetrate a larger depth into the drop than at $t=0.01$: this deeper penetration is marked near the rear stagnation point: see Fig. 13(b). The neighbourhood of the internal stagnation point is still virtually untouched by the mass transfer.

As time progresses beyond $t=2/Pe$ we expect to see a change away from radial gradients: this is in line with the findings of Figs. 4 and 5 which indicated a clear difference between circulating and rigid drop data emerging around this time. This expectation is borne out by data for $t=0.05$ (i.e. $5/Pe$): see Fig. 13(c). There is clear evidence of advection of mass up the drop axis: material has certainly been advected as far as the drop centre. Moreover the contour enclosing the drop centre also encloses the point $r=0.25$ in the equatorial plane: there is therefore evidence for mass being advected along the axis in a relatively thick streamtube, as was claimed in Section 5.3. Nevertheless advection has still not reached the neighbourhood of the forward stagnation point. Strong non-uniformities in mass fraction w_1 along streamlines still persist. Significant changes in mass fraction in the neighbourhood of the internal stagnation point are also starting to appear.

By time $t=0.1$ (i.e. $10/Pe$) the contours of mass fraction start to form closed loops indicating that mass has now been advected along a full streamline orbit: see Fig. 13(d). Moreover to a rough approximation, the streamlines match with the contours of mass fraction, with only slight irregularities in the latter. Since all points along a streamline are now (roughly) equivalent in terms of mass fraction, the evolution of the system no longer depends on how quickly fluid elements orbit their streamlines (i.e. upon Peclet number). It is therefore plausible that for time $t=10/Pe$ onwards the system evolves onto a master curve independent of Peclet number, as Figs. 4 and 5 already suggest.

For $Pe=100$, at the time $t=0.1$ shown in Fig. 13(d), the mass fraction at the internal stagnation point is about half-way to equilibrium. Although not shown in Fig. 13, as time progresses beyond $t=0.1$, the aforementioned irregularities in contours of mass fraction are smoothed out, but the mass fraction also becomes increasingly uniform over the entire drop.

5.5.2. Contour plots for $Pe=1000$

Fig. 14 shows data for $Pe=1000$. Compared to Fig. 13 (with $Pe=100$), there is a greater separation in the time scales for advection (fast) and diffusion (slow). This makes it far easier to distinguish these effects when considering contour plots. Times $t=0.002$, 0.005, 0.01, 0.02, 0.05 and 0.1 are shown.

At time $t=0.002$ (i.e. $2/Pe$), Fig. 14(a) shows similar features to Fig. 13(a), (b), i.e. gradients primarily in the radial direction confined near to the drop surface. The actual gradients in Fig. 14(a) are much larger than in Fig. 13(a), (b), due to the shorter time $t=0.002$ to which Fig. 14(a) corresponds.

By time $t=0.005$ (i.e. $5/Pe$), in Fig. 14(b), we see a change away from wholly radial gradients. Again (compare Fig. 13(c) also at $5/Pe$) material has been advected up the drop axis to the drop centre, but not all the way to the forward stagnation point. Mass fractions are not yet uniform along streamlines.

It is clear in Fig. 14(b) that concentration gradients at the drop surface are substantially larger than those in the vicinity of the drop axis. We expect gradients to be confined to streamlines that pass within an extremely small distance $O(Pe^{-1/2})$ of the surface, and (see Section 5.2) on geometric grounds, these same streamlines pass within a somewhat larger distance $O(Pe^{-1/4})$ of the axis. Given the small gradients near the axis, individual fluid elements experience little mass transfer as they migrate along it (as Fig. 11 also shows).

Another feature of Fig. 14(b) is that mass has travelled slightly further along streamlines which are adjacent to the axis than along the axis itself. This is a manifestation of the different orbit times of different streamlines. The streamlines which carry mass most rapidly into the drop interior are those passing within $O(Pe^{-1/2})$ of the surface (so as to collect material in the first place), but which simultaneously do not pass too near the rear stagnation point, where their orbits would otherwise be held up for long times. Having been carried by streamlines adjacent to the axis, material cannot readily diffuse across to the axis itself, since (for $Pe=1000$) the orbit time is just too short.

Fig. 14(c) shows the mass fraction contours for $t=0.01$ (i.e. $10/Pe$). As in Fig. 13(d), we now see the contours starting to form closed loops. To a quite good approximation streamlines and mass fraction contours match one another (despite some small irregularities in the

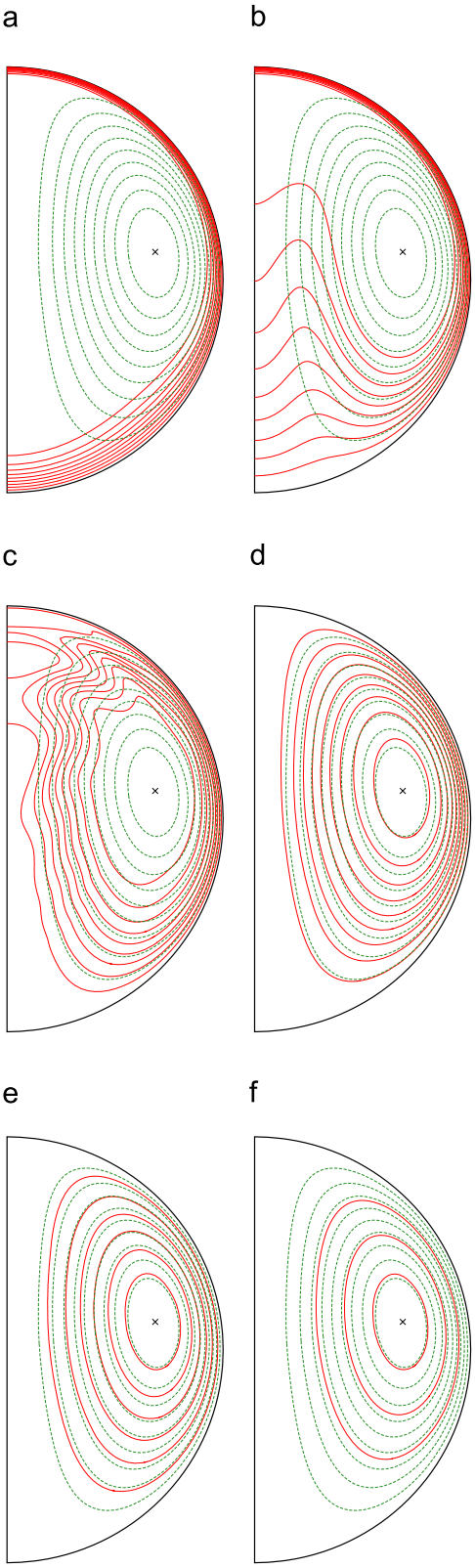

Fig. 14. Contours of mass fraction w_1 for Pe=1000 at times (a) t=0.002, (b) t=0.005, (c) t=0.01, (d) t=0.02, (e) t=0.05 and (f) t=0.1. The contours are as per Fig. 13: the values of w_1 at the internal stagnation point are (a)–(c) 0.200, (d) 0.204, (e) 0.232, and (f) 0.265. The streamline pattern is superposed on each plot.

latter). Moreover (see Fig. 14(d)) the irregularities are smoothed out by time t=0.02 (i.e. 20/Pe).

It is apparent from Fig. 14(c) that for t=0.01 and beyond, mass fraction is effectively uniform along streamlines, and (by implication) the mass fraction should evolve onto a master curve independent of Peclet number. Although Figs. 13(d) and 14(c) show the emergence of closed loop contours, both corresponding to t=10/Pe for their respective Peclet numbers, there are differences between the contour patterns due to the different actual values of t (i.e. 0.1 vs 0.01). In Fig. 13(d), mass fraction at the internal stagnation point has changed markedly from its initial value, whereas in Fig. 14(c) the neighbourhood of the internal stagnation point remains virtually untouched.

For Pe=1000, it is necessary to reach t=0.05 (Fig. 14(e)) to see significant changes in mass fraction at the internal stagnation point. By t=0.1 (see Fig. 14(f)), mass fraction at the internal stagnation point is about halfway to equilibrium. As far as the mass fraction at the internal stagnation point is concerned, there is not much difference between Fig. 13(c) (Pe=100) and Fig. 14(e) (Pe=1000), nor between Fig. 13(d) (Pe=100) and Fig. 14(f) (Pe=1000). We deduce that mass transfer to the internal stagnation point is diffusively controlled, and not sensitive to Peclet number (provided Pe is large enough to establish, in the first place, a state where mass is advected uniformly along individual streamlines before the entire drop equilibrates diffusively).

6. Discussion

Full numerical simulations of the (multi-component) mass transfer process in a circulating fluid drop have demonstrated that mass transfer proceeds and equilibrates more rapidly (by a factor of roughly three) than for a rigid (i.e. non-circulating) drop (Negri and Korchinsky, 1986; Negri et al., 1986). However, mass transfer in the simulations proceeds considerably more slowly (by a factor on the order of roughly 10) than is predicted by boundary layer mass transfer models (Uribe-Ramirez and Korchinsky, 2000a, b).

The boundary layer models assume the drop interior is well-mixed (and this keeps concentration gradients sharp near the surface). Such an assumption might be appropriate for a turbulent flow within and around the drop, but may be invalid if the local drop-scale flow is laminar. In fact the full simulations (with laminar flow) show that material does not exchange mass efficiently in the interior: as a result, concentration gradients become less sharp over time.

Typically in liquid–liquid extraction systems of physical interest, circulation is rapid compared to diffusion. The circulation time is order R/U_{drop} (R is drop radius, and U_{drop} is drop velocity), while the diffusion time is $R^2/\langle D^0\rangle$ ($\langle D^0\rangle$ is the diffusivity scale). The ratio between the diffusion time and circulation time is the Peclet number Pe, and is usually large (e.g. in the range of tens of thousands): fluid elements circulate many times around the drop before equilibrium is reached. If times are made dimensionless on the scale $R^2/\langle D^0\rangle$, then (dimensionless) circulation times are $O(1/Pe)$, which is a small quantity. Under these conditions, the evolution of bulk mass fractions (being the quantities of primary interest to the chemical engineer) becomes, after a (dimensionless) time of roughly $10/Pe$, independent of the speed of the circulation. From this time onwards, up to a dimensionless time of around 0.2 (being the time at which mass fractions effectively equilibrate), Pe is no longer a relevant parameter. For the typical drop radius R (10^{-3} m), drop velocity U_{drop} (0.03 m s^{-1}) and diffusivity scale $\langle D^0\rangle$ (3.48×10^{-9} m^2 s^{-1}) used here, the droplet needs on the order of 60 s of physical time to equilibrate, but reaches a Pe-independent state in less than 1 s. It would no longer be necessary to simulate the mass transfer process at the actual/original Peclet number of interest. Without loss of accuracy, one could switch to much cheaper simulations with a substantially smaller Pe (and a considerably larger simulation time step).

Switching to simulations with $Pe=1000$ is certainly possible, with effectively no change in bulk mass fraction predictions, and even $Pe=100$ gives a fair indication of the behaviour on the approach to equilibration.

A chemical engineer wants to reduce the equilibration time, e.g. from 60 s quoted above to a lesser value e.g. 10 s typical of the contact time between a drop and the surrounding continuous phase in experiments (Uribe-Ramirez and Korchinsky, 2000a; Steiner et al., 1990). According to the current calculations, after 10 s (corresponding to about 0.03 units of dimensionless time), the system is only about halfway to equilibrium: up to twice as much mass transfer can potentially be achieved for the same 10 s experimental contact time, provided the equilibration time can be reduced. According to the simulations, changing Pe number (e.g. by changing U_{drop}) is not a practical way of reducing the equilibration time, since much of the equilibration process is Pe-independent. Instead, reducing drop radius will be more effective (as time is scaled by $R^2/\langle D^0 \rangle$ throughout here).

Looking at the details of the mass fraction evolution at specific spatial locations (instead of merely at bulk mass fractions) helps to elucidate further what is happening in the circulating drop. There is a considerable difference in the evolution of mass fractions on or near the drop axis compared to the evolutions elsewhere (e.g. in the drop equatorial plane).

Points on or near the drop axis evolve on advective time scales. Fluid elements that are originally near the drop surface can exchange mass rapidly there, and then enter the drop interior to travel up the drop axis with limited further mass exchange (or a greatly reduced rate thereof).

By contrast, points off the axis (e.g. in the equatorial plane) evolve much more slowly, i.e. primarily on a diffusive time scale (although small secondary oscillations can be superposed on this diffusive evolution on scales that correlate with streamline orbit times). There is inherently a large separation between the diffusive and advective time scales, since the Peclet number (which is large) is (by definition) the ratio of these scales.

Off the drop axis, the locations which evolve slowest are those which are closest to the drop internal stagnation point, suggesting that mass transfer proceeds from streamline to streamline, with the streamline passing along the drop surface and axis responding first, and those neighbouring the internal stagnation point responding last. Such cross-stream mass transfer is necessarily diffusive, since advection is (by definition) in the streamwise direction only.

Mass fractions should become fairly uniform along a streamline once fluid elements have executed one full streamline orbit: contour plots of mass fraction throughout the drop show that such a state emerges around time $t \approx 10/Pe$.

Given mass fractions are uniform along streamlines, but vary from streamline to streamline, a new description of the mass transfer process is possible (see Appendix B for details of the new model, although the implementation is left for further work). Mass transfer can be described via a one-dimensional diffusion process in a generalised streamfunction space, instead of an advection–diffusion process in spherical coordinates. An effective diffusivity appears in the description, varying from streamline to streamline. The effective diffusivity depends on how streamlines are laid out in space (and thereby depends on fluid mechanical parameters e.g. the Reynolds number), but does not depend directly on the Peclet number, which ceases to be a relevant parameter. It is no longer necessary for a mass transfer simulation to resolve motion of individual fluid elements around streamline orbits: much larger computational time steps become possible than for a full simulation of the original advection–diffusion equation, even a full simulation with a modest Peclet number, e.g. $Pe=100$. Physically, the time for the drop to equilibrate scales diffusively, as is also the case for the rigid drop, but the distance over which diffusion must proceed (from the surface and axis into the internal stagnation point) is less than what occurs for the rigid drop (from the surface to the centre): this is what enables the circulating drop to equilibrate faster than the rigid drop does.

The conclusion that a cross-stream diffusion theory of mass transfer (as outlined in Appendix B) is feasible, is a *general* one, following only from the requirement that the Peclet number be large. The general conclusion is not sensitive to whether we describe the streamline pattern approximately (using a truncated Galerkin expansion for flow within a spherical drop, as has been done here) or more accurately (using e.g. numerical techniques to obtain the flow field, Juncu, 1999; Yan et al., 2002). The *details* of the cross-stream diffusion theory do, however, depend on how accurately the streamline pattern is obtained: in particular the precise value of the effective diffusivity for each streamline depends on the streamline layout. Nevertheless the general conclusion regarding the cross-stream diffusion theory does not even depend on the assumption of drop sphericity (employed throughout our analysis): one could quite easily apply the formalism of Appendix B to a steady state, laminar streamline pattern for a drop of any non-spherical shape.

7. Conclusions

Mass transfer in a circulating drop is challenging to simulate because the process typically occurs at a large Peclet number Pe, thereby with an inherently large ratio between the diffusion time scale (long) and the circulation time scale (short). Insights into the mass transfer behaviour in the high Peclet number regime can be gained by studying a sequence of simulations with increasing Peclet numbers (e.g. $Pe=100$, 1000 and 10 000), but find that a realistic simulation needs to resolve individual circulations (rapid), even though equilibration takes place on the diffusion time scale (slow).

Despite this ultimate diffusive control of the mass transfer, the circulating drop still equilibrates faster than the rigid drop (which is by definition wholly diffusive). For the circulating drop, material is transported rapidly along streamlines, and only needs to diffuse between the surface and an internal stagnation point of the streamline pattern. This gives a lesser diffusion distance than the rigid drop (where material diffuses between the surface and the centre) and hence a more rapid equilibration time (roughly by a factor of about three).

The circulating drop numerical simulations likewise do not agree well with boundary layer models of mass transfer, such as those of Uribe-Ramirez and Korchinsky (2000a, b), which themselves attempt to take account of circulation. Whereas the rigid drop equilibrated too slowly, the boundary layer models equilibrate much more rapidly (compared to the circulating drop simulations). For a typical drop Peclet number of $Pe=10\,000$, the boundary layer models predict higher estimates of the rate of equilibration by a factor on the order of roughly 10. The reason for this is that the boundary layer models assume that solute concentration gradients near the drop surface are kept sharp owing to perfect mixing in the bulk of the drop. Instead the full numerical simulation finds that mass transfer in the bulk is far from perfect: as a result, cross-stream concentration gradients at the drop surface do not remain sharp. Instead these gradients decay over time, and mass transfer rates correspondingly decay.

For consistency with previous work (Korchinsky et al., 2009), a multi-component mass transfer model has been used throughout here. In fact, the multi-component effects can be shown to be quite weak: the off-diagonal components of the multi-component Fick diffusivities are much smaller than the diagonal ones in Eq.

(15). In these circumstances, the multi-component process will typically behave like two independent single-component transfers. Inherently multi-component effects only become evident if the difference imposed between initial and final mass fractions for one component (e.g. component 1) are much larger than those for another (e.g. component 2). Then the diffusive flux of component 2 can be affected by the (large) imposed gradient of component 1 multiplied by a (small) off-diagonal Fick diffusivity, in addition to the (small) imposed gradient of component 2 multiplied by a (larger) diagonal Fick diffusivity. This inherently multi-component case is left for further work.

Acknowledgements

S. Ubal acknowledges support from Consejo Nacional de Investigaciones Cientificas y Tecnicas (CONICET) and EPSRC Contract EP/D062128/1.

Appendix A. The boundary layer mass transfer model

The purpose of this appendix is to explain in detail the boundary layer mass transfer model of Uribe-Ramirez and Korchinsky (2000a, b). The discussion given originally by Uribe-Ramirez and Korchinsky focussed on the mathematical solution of the model, but offered much less in the way of physical interpretation. Even though, in the main text, the boundary layer model predictions were found to differ substantially from those of the full numerical simulations of mass transfer, an in depth discussion of the Uribe-Ramirez and Korchinsky model is still warranted here. A detailed physical understanding of the boundary layer model explains how the substantial differences (compared to the numerical simulations) come about. Moreover a deep physical understanding of the model shows that it is still potentially very useful for describing the mass transfer process at early times (comparable with the timescale of the orbit of a typical fluid element around the drop), which are challenging to simulate numerically (owing to the extremely thin layers arising at those times). The discrepancies observed in the main text between the boundary layer model and the full numerical simulations arise because Uribe-Ramirez and Korchinsky attempted to utilise the boundary layer model for times far longer than would be permissible (at least using the set of conditions they assumed).

The notation to be employed here differs slightly from that originally used by Uribe-Ramirez and Korchinsky (2000a, b). The additional physical insights to be offered here have enabled us to simplify a number of terms which were left unsimplified in Uribe-Ramirez and Korchinsky's original work, and also to introduce some a priori simplifications (of expressions which Uribe-Ramirez and Korchinsky only eliminated after considerable algebraic effort). Collectively these simplifications have spurred the notational changes. The development below *is* equivalent to Uribe-Ramirez and Korchinsky's work, even though this is not immediately obvious by a cursory comparison of the various formulae derived. Extensive use of trigonometric identities is actually required to demonstrate formal equivalence between Uribe-Ramirez and Korchinsky's formulae (in their unsimplified form) and those formulae to be presented here.

The rest of this appendix is laid out as follows. Section A.1 develops the equations of the boundary layer model, while Section A.2 discusses a similarity solution. Section A.3 discusses a key variable appearing in the solution, to be called the 'extent of diffusion'. Sections A.4–A.6 consider formulae for the 'extent of diffusion', in general, as well as in the limit of very early times and at later times. Section A.7 applies the boundary layer model to predict the evolution of bulk drop mass fractions: these predictions are the ones compared against the full numerical simulations in the main text. Section A.8 generalises the results from single-component to multi-component mass transfer.

A.1. Equations of the boundary layer model

Consider in the first instance a single component (mass fraction w_1) being convected around a circulating drop and also diffusing.

The governing convection–diffusion equation is

$$\frac{\partial w_1}{\partial t} + Pe\,\boldsymbol{u}\cdot\nabla w_1 = \Delta_{11}\nabla^2 w_1. \tag{A.1}$$

This equation is in dimensionless form, using the same scalings as in the main text. The value Δ_{11} is the diffusivity ratio between solute at the actual mass fraction of interest and at infinite dilution. In line with the main text, Δ_{11} is assumed constant and uniform for the purposes of solving Eq. (A.1); it has an $O(1)$ value, but generally speaking is not precisely unity.

Again as in the main text, the velocity field $\boldsymbol{u}$ in the radial and axial directions is defined in terms of streamfunction ψ via Eqs. (6) and (7). Recall that, by convention $\psi=0$ on the drop surface r=1. Remember also the sign convention here: ψ is considered to be positive in the interior of the drop (so that, by Eq. (7), u_θ is positive on the surface).

Instead of standard spherical coordinates, we choose a coordinate system (ψ, s, ϕ) where ψ is the streamfunction itself, s is distance measured along a streamline and ϕ is azimuthal angle (there is ultimately no dependence on ϕ as the system is axisymmetric).

In this new coordinate system, the governing convection–diffusion equation becomes (recognising that convection is, by definition, solely along streamlines at speed u_s say, and also that, in a boundary layer system, diffusion is primarily across streamlines, i.e. radially near the drop surface)

$$\frac{\partial w_1}{\partial t} + Pe\,u_s\frac{\partial w_1}{\partial s} = \Delta_{11}u_\theta\frac{\partial}{\partial\psi}\left(u_\theta r^2\sin^2\theta\frac{\partial}{\partial\psi}w_1\right), \tag{A.2}$$

where Eq. (7) has been used on the right-hand side.

Recall that, in the above, time has been made dimensionless on a diffusive scale. It is possible to define a new dimensionless time variable, denoted T say, which is made dimensionless on a convective scale. In fact

$$T = Pe\,t. \tag{A.3}$$

One streamline orbit of a typical streamline corresponds to $O(1)$ units of convective time T, but much less than one unit of diffusive time t (remember $Pe \gg 1$ here). Moreover within a boundary layer on the drop surface ($r\approx 1$), the coordinate s (distance along a streamline) can be taken to be synonymous with the polar angle θ. Moreover $\sin\theta$ and u_θ vary along (but not across) the boundary layer, and u_θ can be approximated by its value on the drop surface denoted $u_{\theta|surf}$ (a function solely of θ). Hence from Eq. (A.2), we deduce

$$\frac{\partial w_1}{\partial T} + u_{\theta|surf}\frac{\partial w_1}{\partial\theta} = \frac{\Delta_{11}}{Pe}u_{\theta|surf}^2\sin^2\theta\frac{\partial^2}{\partial\psi^2}w_1. \tag{A.4}$$

Our aim is to solve this equation for w_1 in terms of ψ, θ and T.

A.2. Similarity solution of the boundary layer model

Uribe-Ramirez and Korchinsky proposed that the above equation could be solved in terms of a similarity solution

(Uribe-Ramirez and Korchinsky, 2000a),

$$w_1 = w_1^R + (w_1^{inject}(T_r(T,\theta)) - w_1^R)\mathrm{erf}\left(\frac{\psi\sqrt{Pe}}{\sqrt{4\Lambda_{11}\zeta(T,\theta)}}\right), \quad (A.5)$$

where w_1^R represents an imposed mass fraction on the drop surface (for convenience here assumed to be fixed in time; Uribe-Ramirez and Korchinsky considered more general cases), while w_1^{inject} (allowed to vary with time) is the mass fraction of material being injected from the drop interior onto the surface. Meanwhile T_r (the argument of the function w_1^{inject}) is a so-called retarded time function: it represents the time at which a fluid element currently on the drop surface at angular position θ is considered to have first reached the surface. Meanwhile ζ is a function which we call the 'extent of diffusion': it determines (at any given T and θ) how many streamlines have been affected by the diffusion. More explanation of the functions T_r and ζ is now given.

A fluid element which is initially on the drop surface, and which is continuously on the surface for subsequent times, has (by definition) $T_r \equiv 0$. Such elements also have (by definition) $w_1^{inject} \equiv w_1^0$, with w_1^0 being the uniform initial mass fraction inside the drop. Meanwhile, for an element injected on to the surface from the interior after the initial time, the retarded time function is defined

$$T_r = T - \int_{\theta_i}^{\theta} \mathrm{d}\theta / u_{\theta|surf}, \quad (A.6)$$

where θ_i is the angular position at which fluid elements are considered to be injected onto the surface from the interior (see Fig. 15). The integral $\int_{\theta_i}^{\theta} \mathrm{d}\theta/u_{\theta|surf}$ is the transit time along the surface from angle θ_i to angle θ.

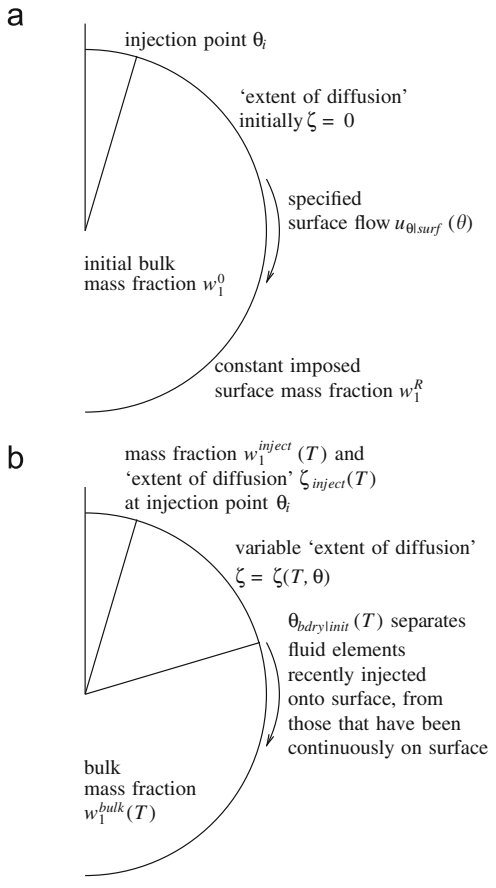

Fig. 15. Definition sketch for Uribe-Ramirez and Korchinsky surface boundary layer model (a) indicating initial conditions and/or quantities which are held constant over time, (b) indicating quantities which vary over time.

There are technical mathematical difficulties associated with choosing $\theta_i = 0$ (as the poles of the drop are stagnation points—a boundary layer picture relying on fast circulation along the drop surface is locally invalid there). However, almost any arbitrary non-zero value of θ_i satisfying $\theta_i \ll 1$ can be a sensible choice—indeed the formulae derived by Uribe-Ramirez and Korchinsky are insensitive to the choice of θ_i (since those formulae are subsequently applied on time scales much longer than that of a typical streamline transit/orbit).

Physically Eq. (A.6) says that T_r is tied to fluid material elements. Mathematically this leads to considerable simplification and cancellation when a solution of the form of Eq. (A.5) is substituted into Eq. (A.4).

An equation for the so-called 'extent of diffusion' ζ can now be derived via Eqs. (A.4) and (A.5). This is found to be

$$\partial\zeta/\partial T + u_{\theta|surf}\partial\zeta/\partial\theta = u_{\theta|surf}^2 \sin^2\theta. \quad (A.7)$$

Uribe-Ramirez and Korchinsky analysed this equation mathematically, but offered little physical interpretation of either the equation itself or of the solution ζ. Understanding these concepts is key to interpreting their entire boundary layer model, as is explained in the next section.

A.3. Interpretation of the 'extent of diffusion'

In their mathematical method, Uribe-Ramirez and Korchinsky identified (and solved for ζ along) so-called characteristic curves in the θ, T plane which had particular well defined values of $\mathrm{d}\theta/\mathrm{d}T$. However, Uribe-Ramirez and Korchinsky did not point out that the well defined values of $\mathrm{d}\theta/\mathrm{d}T$ were in fact equal to $u_{\theta|surf}$—this means that all points on a given characteristic curve correspond to a given fluid element/material point. Thus the values of ζ which Uribe-Ramirez and Korchinsky determined on their characteristic curves were in fact values of ζ following material points.

Eq. (A.7) written for a material point becomes

$$\mathrm{D}\zeta/\mathrm{D}T = u_{\theta|surf}^2 \sin^2\theta. \quad (A.8)$$

The physical interpretation is as follows: ζ is a variable which accumulates as diffusion proceeds, somewhat like time T. However, while T is a 'clock' that advances at a fixed rate, ζ is a 'clock' that can run either fast or slow depending on circumstances (specifically depending on the values of $u_{\theta|surf}$—i.e. kinematics—and $\sin\theta$—i.e. geometric location). A very loose analogy can be drawn with Einstein's theories of special (Einstein, 1905) and general (Einstein, 1916) relativity, in which clocks run at different rates depending on kinematics and geometry.

Remembering that (in the vicinity of the drop surface $r=1$) we have $\partial\psi/\partial r = -u_{\theta|surf}\sin\theta$, we deduce

$$\mathrm{D}\zeta/\mathrm{D}T = (\partial\psi/\partial r)^2. \quad (A.9)$$

Thus the rate at which ζ advances is inversely proportional to the square of the distance between adjacent streamlines. Diffusion in the Uribe-Ramirez and Korchinsky boundary layer is from streamline to streamline, and if streamlines move apart, we expect the rate of diffusion to fall as the inverse square of the separation distance (as is standard for diffusive systems).

The streamlines can move apart for either of two reasons as identified above—a kinematic effect (streamlines move apart near surface stagnation points where $u_{\theta|surf}$ is small, as there is less fluid circulation there), and a geometric one (streamlines move apart near the axis where $\sin\theta$ is small, as there is less volume there). These two effects cooperate in the circulating drop, since there are stagnation points ($u_{\theta|surf} \to 0$) on the axes ($\theta = 0$ or $\theta = \pi$) at the poles.

In summary the rate of advance of ζ increases and decreases precisely as the rate of diffusion rises or falls. All the above implies that ζ is a 'diffusive clock' which keeps track of the accumulated 'extent of diffusion'.

A.4. Formula for the 'extent of diffusion'

In order to solve Eq. (A.7) for the 'extent of diffusion' ζ, one needs an initial condition (i.e. ζ as a function of θ for T=0; the function is typically defined from an 'injection' angle $\theta=\theta_i \ll 1$ up to $\theta=\pi$). One also needs a boundary condition (i.e. ζ at $\theta=\theta_i$ as a function of T for $T>0$).

Fluid elements injected from the interior at time zero will reach, at time T, an angular position (denoted $\theta_{bdry|init}(T)$ say) which satisfies the implicit equation

$$T=\int_{\theta_i}^{\theta_{bdry|init}(T)} \mathrm{d}\theta/u_{\theta|surf}(\theta). \tag{A.10}$$

The point $\theta_{bdry|init}(T)$ separates fluid elements which have been recently injected onto the surface since time zero, from those which have been continuously on the surface for all times (see Fig. 15).

If $T \ll 1$ (i.e. much less than a typical streamline orbit duration) then $\theta_{bdry|init}(T)\to\theta_i \ll 1$: the vast majority of surface elements have been continuously on the surface at all times. On the other hand, if T is significantly greater than unity (i.e. greater than a typical streamline orbit) then $\theta_{bdry|init}\to\pi$ (assuming there are no other stagnation points on the surface streamline other than at the poles): the vast majority of surface fluid elements have been injected onto the surface since time zero. We consider those two cases in turn.

A.5. Solution for ζ at early times

If $T \ll 1$ then the value of θ for a given surface fluid element will not change significantly between time zero and time T.

If we assume that initially no diffusion has taken place (i.e. the initial condition for ζ is $\zeta\equiv 0$) then the resulting solution of Eq. (A.7) for ζ is

$$\zeta \approx (u_{\theta|surf}^2 \sin^2\theta)\, T. \tag{A.11}$$

Assuming (as before) the uniform initial mass fraction inside the drop is denoted w_1^0, Eq. (A.5) then becomes

$$\begin{aligned} w_1 &= w_1^R + (w_1^0 - w_1^R)\,\mathrm{erf}\,\frac{\sqrt{Pe}\,\psi}{u_{\theta|surf}\sin\theta\sqrt{4\Delta_{11}T}} \\ &= w_1^R + (w_1^0 - w_1^R)\,\mathrm{erf}\,\frac{(1-r)}{\sqrt{4\Delta_{11}t}}, \end{aligned} \tag{A.12}$$

where we have used Eqs. (7) and (A.3).

Eq. (A.12) corresponds to the boundary layer result (i.e. the similarity solution alluded to in Section 2.1) for early times for a rigid (i.e. non-circulating) drop. The reason is that, at the early times in question, the drop circulation has not yet manifested itself—surface fluid elements have not moved significantly from their original positions. There has been so little turnover of surface fluid that essentially all surface fluid elements have been continuously on the surface at all times (as is also the case for a rigid drop).

A.6. Solution for ζ at longer times

If $T \geq O(1)$, there has already been considerable turnover of surface fluid ($\theta_{bdry|init}(T)\to\pi$). This is the limit studied by Uribe-Ramirez and Korchinsky.

The initial distribution of ζ on the drop surface (as a function of θ) is no longer relevant to the solution. However, the time history of ζ at the injection point (i.e. the boundary condition for ζ at $\theta=\theta_i$) now is relevant.

Suppose the time history at the injection point is denoted by a function $\zeta_{inject}(T)$. Then the solution of Eq. (A.7) for $\zeta(T,\theta)$ is

$$\zeta = \zeta_{inject}(T_r) + \int_{\theta_i}^{\theta} u_{\theta|surf}\sin^2\theta\,\mathrm{d}\theta. \tag{A.13}$$

Note that ζ_{inject} in the above equation is evaluated at the retarded time T_r not at the current time T: here T_r depends on T and θ (see Eq. (A.6)).

Uribe-Ramirez and Korchinsky were interested in solving Eq. (A.7) for a particular simple $u_{\theta|surf}$ function obtained from a drastically truncated Galerkin expansion (see e.g. Eqs. (5)–(7)) of the Navier–Stokes equations. Analytic integration of Eq. (A.13) was then possible utilising a well-known substitution technique (called the t-substitution, Stroud and Booth, 2001; see also Green et al., 2006; Grassia et al., 2008; Cox et al., 2009 which have utilised the technique recently): solutions for ζ were then expressed analytically in terms of $\tan\theta/2$, but were quite unwieldy.

The formula supplied by Uribe-Ramirez and Korchinsky (2000a) also contained an analytic expression (in terms of T and θ) for the argument T_r of $\zeta_{inject}(T_r)$. This can be obtained via Eq. (A.6) again using the t-substitution, although note there is actually a minor typographical error in the integrated expression for T_r (Eq. (65) in the cited reference).

The analytic forms of the solutions for ζ and T_r, whilst undoubtedly useful, tend to obscure the rather simple origin of the solutions, namely Eqs. (A.13) and (A.6), respectively. For any given flow field $u_{\theta|surf}$, the integrals in these equations could easily be obtained by numerical quadrature rather than analytic integration. Indeed in some ways using numerical quadrature is more robust than analytic integration: one is no longer tied to the surface flow field given by e.g. a Galerkin expansion, but rather one can use $u_{\theta|surf}$ values for flow fields computed via more accurate numerical procedures (see e.g. Juncu, 1999; Yan et al., 2002).

Uribe-Ramirez and Korchinsky supposed that fluid elements in the bulk of the drop were well mixed (see Fig. 2), arriving at the injection point with $\zeta=0$. Effectively the 'diffusive clock' which ζ represents is reset to zero in the drop interior. Since the function ζ_{inject} in Eq. (A.13) is now identically zero, the fact (noted above) that the original reference contained typographical errors in the argument of this function has no bearing on the predictions.

Time dependence now drops out of Eq. (A.13): ζ depends solely on θ,

$$\zeta = \int_{\theta_i}^{\theta} u_{\theta|surf}\sin^2\theta\,\mathrm{d}\theta. \tag{A.14}$$

By contrast with Eq. (A.6) where θ_i was necessarily non-zero, it is permitted in Eq. (A.14) to take $\theta_i\to 0$. The reason for this can be understood by recalling that ζ measures the 'extent of diffusion'. Diffusion proceeds from streamline to streamline, but streamlines are so far apart in the vicinity of the poles of the drop (see Section A.3), that effectively no diffusion occurs for $\theta\to 0$ (even though fluid elements are held up for long times there).

Note that the well-mixed assumption that $\zeta_{inject}\equiv 0$ (while mathematically convenient, and possibly even valid physically for a turbulent drop) is not an absolutely essential part of the boundary layer model. For instance, in a drop with laminar flow, it would be quite possible to impose a boundary condition of $\zeta=0$ at $\theta=\theta_i$ for times up to and including one typical streamline orbit, with the boundary value of ζ jumping to a non-zero value after

this. Physically this could imply that fluid elements which pass along the drop surface, enter the drop interior to migrate up the axis, and then return to the drop surface, 'remember' the value of ζ that they had when they originally left the drop surface. This means that efficient mass transfer (i.e. 'mixing') is not taking place in the interior (on purely geometric grounds, streamlines necessarily spread out near the drop axis, limiting their ability to exchange mass diffusively amongst themselves), and that actually matches much better with the predictions of the full numerical simulations than the well-mixed assumption of Uribe-Ramirez and Korchinsky does.

Employing the well-mixed assumption is what causes the predictions of mass transfer in the Uribe-Ramirez and Korchinsky model to evolve (as was seen in the main text) much too quickly compared to the full numerical simulations. We consider these mass transfer rate predictions in the next subsection.

A.7. Mass transfer rate from drop and bulk mass fractions within drop

The mass flux from any point on the drop surface is $-\Delta_{11}\partial w_1/\partial r|_{r=1}$. Integrating this over the surface gives the total mass transfer rate from the drop. Suppose w_1^{bulk} denotes the mass fraction in the drop averaged over drop volume. Clearly $\mathrm{d}w_1^{bulk}/\mathrm{d}t$ depends on the total surface mass transfer rate. Given that the drop volume is $4\pi/3$, and given Eq. (A.5) we find

$$\frac{\mathrm{d}w_1^{bulk}}{\mathrm{d}t} = Pe\,\frac{\mathrm{d}w_1^{bulk}}{\mathrm{d}T} = -\frac{3}{2}\frac{\sqrt{Pe\,\Delta_{11}}}{\sqrt{\pi}}\int_{\theta_i}^{\pi}(w_1^{inject}(T_r(T,\theta))-w_1^R)\frac{u_{\theta|surf}\sin^2\theta}{\sqrt{\zeta(T,\theta)}}\,\mathrm{d}\theta. \tag{A.15}$$

Note that the lower integration limit here is the injection point $\theta=\theta_i$. We are ignoring a small fraction of the drop surface near the pole $0\le\theta\le\theta_i$. This, however, contributes negligibly to mass transfer, firstly because there is negligible surface area near the pole, and secondly because streamlines are far apart there, and so cross-stream diffusive fluxes are small.

In order to proceed further, it is necessary to find an expression for w_1^{inject}. If T is up to the duration of a typical streamline orbit (or at the very least up to the passage time of a typical fluid element up the drop axis), it should be possible to assume $w_1^{inject}(T)=w_1^0$ (since any material injected at sufficiently early times must have originally come from the drop interior and has never been in proximity to the surface). In that case, Eq. (A.15) (coupled to Eqs. (A.6) and (A.14)) should give quite reliable predictions for total mass transfer rates from the drop. Alternatively if the drop is considered well mixed (as in the work of Uribe-Ramirez and Korchinsky), we have (for all times T, including times longer than a typical streamline orbit)

$$w_1^{inject}(T)\equiv w_1^{bulk}(T). \tag{A.16}$$

Again note that the drop being well-mixed is an assumption, not an essential feature of the boundary layer model. Consider e.g. yet another alternative of a fluid element which travels along the drop surface (acquiring a mass fraction near w_1^R), which then enters the interior of the drop to travel up the drop axis (without exchanging much mass with other fluid elements) and which is then reinjected onto the drop surface at angle θ_i. Upon reinjection w_1^{inject} will jump abruptly with time from a value near the initial mass fraction w_1^0 to a value much closer to w_1^R. Clearly from Eq. (A.15), the total mass transfer rate will dramatically decrease. In the absence of good mixing, the jump in w_1^{inject} will also coincide (see Section A.6) with an upwards jump in the function ζ, as reinjected fluid elements fail to reset their 'diffusive clocks'. This contributes yet further to the decay in total mass transfer rate in Eq. (A.15).

Suppose now that the well-mixed assumption (i.e. Eq. (A.16)) applies. Strictly speaking Eq. (A.15) then becomes an integro-differential equation—the rate of change of w_1^{bulk} at time T depends on the entire time history of w_1^{bulk} (via the retarded time function $T_r(T,\theta)$ defined in Eq. (A.6)), not merely on the instantaneous value of $w_1^{bulk}(T)$.

Uribe-Ramirez and Korchinsky considered the well-mixed model in the limit of large times $T\gg 1$ (i.e. at times much longer than those mentioned above for which it would be reasonable to expect that a boundary layer model would be reliable without the additional assumption of good mixing). In this case ζ becomes a function solely of θ: see Eq. (A.14). It is possible to suppose moreover that w_1^{bulk} evolves on a time scale much greater than that of a typical streamline orbit. Then the distinction between the current time T and the retarded time T_r becomes irrelevant, and we obtain a differential equation

$$\frac{\mathrm{d}w_1^{bulk}}{\mathrm{d}T} = -\frac{3}{2}\frac{\sqrt{\Delta_{11}}}{\sqrt{\pi\,Pe}}(w_1^{bulk}(T)-w_1^R)\int_{\theta_i}^{\pi}\frac{u_{\theta|surf}\sin^2\theta}{\sqrt{\zeta(\theta)}}\,\mathrm{d}\theta = -\frac{3}{\sqrt{\pi}}\frac{\sqrt{\Delta_{11}\,\zeta(\pi)}}{\sqrt{Pe}}(w_1^{bulk}(T)-w_1^R). \tag{A.17}$$

Eq. (A.14) was used to perform the integral in the argument of the exponential. It is permitted to take $\theta_i\to 0$ as the lower integration limit: both the numerator and denominator of the integrand vanish as $\theta\to 0$, but the numerator tends to vanish more rapidly. The solution of Eq. (A.17) is

$$w_1^{bulk} = w_1^R+(w_1^0-w_1^R)\exp\left(-\frac{3}{\sqrt{\pi}}\frac{\sqrt{\Delta_{11}\,\zeta(\pi)}}{\sqrt{Pe}}\,T\right) = w_1^R+(w_1^0-w_1^R)\exp\left(-\frac{3}{\sqrt{\pi}}\sqrt{\Delta_{11}Pe\,\zeta(\pi)}\,t\right). \tag{A.18}$$

Eq. (A.18) is the formula (along with Eq. (A.14)) ultimately utilised by Uribe-Ramirez and Korchinsky (2000a).

Some comments are pertinent: Eq. (A.18) has been obtained on the basis of a well-mixed model. By continually resetting ζ to zero in the bulk of the drop before reinjecting fluid elements onto the surface, the mass transfer boundary layer (across which mass transfer takes place) only has an opportunity to grow during the time that fluid elements sweep around the drop surface. This corresponds to $O(1)$ units of hydrodynamic time T, but only $O(1/Pe)$ units of diffusive time t. Boundary layer thicknesses scale as the square root of the (diffusive) time for which boundary layers are permitted to grow: for $O(1/Pe)$ growth time, boundary layers are therefore maintained at $O(Pe^{-1/2})$ maximum thickness. Concentration gradients are kept sharp and mass transfer proceeds at a rapid rate, as can be seen by the factor $\sqrt{Pe}$ in the argument of the exponential in Eq. (A.18)—the other factors in the argument $\sqrt{\Delta_{11}}$ and $\sqrt{\zeta(\pi)}$ (the latter being computed either via quadrature or analytically) are both order unity. For our selected flow field, specified by Eq. (5) with Galerkin coefficients (8)–(13), we can evaluate Eq. (A.18) as

$$w_1^{bulk} = w_1^R+(w_1^0-w_1^R)\exp(-1.50\sqrt{\Delta_{11}Pe\,t}). \tag{A.19}$$

The situation described by Eq. (A.18) and/or Eq. (A.19) should be contrasted with the full numerical simulations during which mass transfer boundary layers continually thicken over time, and mass transfer rates fall off more dramatically. The well-mixed boundary layer model equilibrates in $O(Pe^{-1/2})$ units of diffusive time (i.e. $O(Pe^{1/2})$ streamline orbits). Meanwhile the full numerical simulations require more time (i.e. up to $O(1)$ units of diffusive time or $O(Pe)$ streamline orbits) to equilibrate.

Another comment concerns the behaviour for very small hydrodynamic times $T \ll 1$ (i.e. outside the range of times for which Eq. (A.18) was derived). In this limit, essentially all surface fluid elements have been continuously on the surface since time zero, and (by the definition given in Section A.2) have T_r=0 and w_1^{inject}=w_1^0. Moreover ζ should be given by Eq. (A.11) rather than Eq. (A.13): the latter equation overestimates ζ, and so overestimates boundary layer thicknesses and underestimates mass transfer rates.

Correcting these estimates, for $T \ll 1$, we find instead

$$w_1^{bulk} \approx w_1^0 - \frac{6}{\sqrt{\pi}} \sqrt{\Delta_{11}} (w_1^0 - w_1^R) \sqrt{t}, \tag{A.20}$$

which can be obtained directly starting from the $T \ll 1$ mass fraction profile Eq. (A.12). We already commented that Eq. (A.12) actually represents the early time concentration profile of a rigid drop (with which the model under discussion here necessarily agrees for $T \ll 1$, such that no significant turnover of fluid on the drop surface has yet occurred): thus Eq. (A.20) represents the early time mass fraction evolution for a rigid drop. On the basis of this limiting behaviour, we conclude that a boundary layer model with surface circulation (as we consider here) can evolve at least as rapidly as a rigid drop, as one would expect physically.

Nevertheless, since all the Uribe-Ramirez and Korchinsky predictions presented in the main text (see e.g. Section 5.1.2) use Eq. (A.18), for $T \ll 1$ they actually evolve *more slowly than* Eq. (A.20), and likewise more slowly than the full numerical simulations (and indeed than the rigid drop predictions) at these times. We emphasise that this incorrect early time evolution obtained by Uribe-Ramirez and Korchinsky is not a feature of the boundary layer mass transfer model per se, but rather due to employing a functional form for ζ which is invalid for $T \ll 1$ (instead a full solution of Eq. (A.7) is required, with initial condition $\zeta = 0$ and boundary condition $\zeta = \zeta_{inject}$, typically with ζ_{inject} itself vanishing); moreover the overall error in drop mass fractions that arises from the early time behaviour Eq. (A.18) is not usually large (since typically we are interested in very large Peclet numbers, such that the period when $T \ll 1$ represents only a very tiny fraction of the full evolution). By contrast, in the long time limit $T \gg 1$, the boundary layer mass transfer model (coupled to a well-mixed assumption in the drop interior) leads to an evolution that is much more rapid than the full numerical simulations, and it is this effect which ordinarily leads to large discrepancies between Uribe-Ramirez and Korchinsky and the full numerical simulations.

A.8. Multi-component case

All the development of Sections A.1–A.7 has concerned the single component case: (Uribe-Ramirez and Korchinsky, 2000b) also considered the full multi-component case. It is clear that single component Eq. (A.1) is mathematically analogous to multi-component Eq. (18), provided we replace w_1 and Δ_{11} in one equation by $\overline{\boldsymbol{w}}$ and $\boldsymbol{\lambda}$ in the other. All the development of Sections A.1–A.7 carries over analogously: details are omitted here.

The main conclusions of Sections A.1–A.7 still apply, i.e. mass transfer boundary layers are still limited to only $O(Pe^{-1/2})$ in thickness, so that concentration gradients are still sharp. The multi-component Uribe-Ramirez and Korchinsky model still equilibrates in $O(Pe^{1/2})$ units of hydrodynamic time, or equivalently in $O(Pe^{-1/2})$ units of diffusive time: this is $O(\mathrm{Pe}^{1/2})$ times faster than the equilibration of the full numerical simulation of the circulating drop (which imposes no upper limit on the thickness of the mass transfer boundary layers, but instead allows these layers to thicken continually over time).

Appendix B. Cross-stream diffusion theory of mass transfer

In the main text we saw that (for large Peclet numbers) from times roughly 10/*Pe* onwards the evolution of the bulk mass fraction became essentially independent of Peclet number (Section 5.1). We also saw that points on streamlines passing near the drop surface and/or the drop axis reached equilibrium much more quickly than points on streamlines passing close to the internal stagnation point (Sections 5.2–5.4). Moreover we saw that mass fractions (from time 10/*Pe* onwards), tended to be uniform along streamlines, but varied across them (Section 5.5). All these indicate that mass is being transferred across streamlines from the surface/axis to the internal stagnation point: see also Fig. 10 showing this process schematically. If mass transfer is wholly (or largely) in the cross-stream direction, the Peclet number, governing the rate at which fluid circulates around streamlines, ceases to be a relevant parameter.

In this appendix we develop equations describing such a cross-stream diffusive process. One could envisage solving a circulating drop problem via a full numerical simulation (as in the main text) and then (from e.g. time 10/*Pe* onwards) switching to the (far more economical) cross-stream diffusion model we now describe. Alternatively one might even be able to dispense with the full numerical simulation altogether: a boundary layer model (of the general type described in Appendix A) could be used on the time scale of an individual streamline orbit, with an immediate switch for subsequent times to the cross-stream diffusion model to be derived and described below. We leave the actual implementation of these 'hybrid' models for further work.

We choose as in Section A.1 a coordinate system where ψ is streamfunction, s is distance along streamlines, and ϕ is azimuthal angle (and as before we look for axisymmetric solutions).

The mass transfer Eq. (14) can be written

$$\frac{\partial \boldsymbol{w}}{\partial t} + Pe\, u_s \frac{\partial \boldsymbol{w}}{\partial s} = \boldsymbol{\Delta} u_s \frac{\partial}{\partial \psi}\left(u_s r^2 \sin^2\theta \frac{\partial \boldsymbol{w}}{\partial \psi}\right) + \boldsymbol{\Delta} u_s \frac{\partial}{\partial s}\left(\frac{1}{u_s}\frac{\partial \boldsymbol{w}}{\partial s}\right). \tag{B.1}$$

This equation is extremely similar to Eq. (A.2) (or at any rate a multi-component version thereof), but we are no longer solving for a surface boundary layer, so we are no longer making the assumption that $\boldsymbol{u}$ is wholly tangential to the drop surface. Moreover we are recognising that $\boldsymbol{w}$ can (in general) vary along streamlines, not merely across them. It is clear from Eqs. (6)–(7) that the speed on streamlines u_s is

$$u_s = (u_r^2 + u_\theta^2)^{1/2} = |\nabla\psi|/(r\sin\theta). \tag{B.2}$$

Since ψ by definition only varies in the cross-stream direction, it is simple to determine via Eq. (B.2) that the distance between adjacent streamlines scales inversely as $u_s r \sin\theta$, and it is on this basis that Eq. (B.1) was derived (starting from Eq. (14)).

Consider an element of length along a streamline ds. The (convective) time taken for a fluid element to pass along this element of length is ds/u_s. The total time (denoted T_{orbit}) taken to orbit once around a streamline is

$$T_{orbit}(\psi) = \oint \frac{\mathrm{d}s}{u_s(\psi, s)}. \tag{B.3}$$

We define a streamline-averaged mass fraction $\boldsymbol{W}$ as

$$\boldsymbol{W}(\psi, t) = \frac{1}{T_{orbit}(\psi)} \oint \frac{\boldsymbol{w}(\psi, s, t)\, \mathrm{d}s}{u_s(\psi, s)}. \tag{B.4}$$

If we multiply Eq. (B.1) by ds/u_s, integrate over a streamline orbit and then divide through by $T_{orbit}(\psi)$ we obtain

$$\frac{\partial \boldsymbol{W}}{\partial t} = \frac{\boldsymbol{\Delta}}{T_{orbit}(\psi)} \frac{\partial}{\partial \psi}\left(\oint \left(u_s(\psi, s) r^2(\psi, s) \sin^2\theta(\psi, s) \frac{\partial}{\partial \psi} \boldsymbol{w}(\psi, s, t)\right) \mathrm{d}s\right). \tag{B.5}$$

In general $\boldsymbol{w}$ (and hence $\partial\boldsymbol{w}/\partial\psi$) depends on s as well as ψ and t. However, if a fluid element must orbit many times around a streamline before reaching its equilibrium mass fraction, it is reasonable to suppose that $\boldsymbol{w}$ might vary only weakly along streamlines. If we can replace $\partial\boldsymbol{w}/\partial\psi$ on the right-hand side of Eq. (B.5) by its streamline averaged counterpart $\partial\boldsymbol{W}/\partial\psi$, further simplification becomes possible. Specifically

$$\frac{\partial \boldsymbol{W}}{\partial t} = \frac{\boldsymbol{\Delta}}{T_{orbit}(\psi)} \frac{\partial}{\partial \psi} \left(D_{eff}(\psi) T_{orbit}(\psi) \frac{\partial \boldsymbol{W}}{\partial \psi} \right), \tag{B.6}$$

where we have defined an effective diffusivity $D_{eff}(\psi)$ for each streamline via

$$D_{eff} = \frac{1}{T_{orbit}(\psi)} \oint u_s^2(\psi, s) r^2(\psi, s) \sin^2\theta(\psi, s) \frac{\mathrm{d}s}{u_s(\psi, s)}. \tag{B.7}$$

The quantity D_{eff} is the streamline-averaged value of the inverse square of the distance between adjacent streamlines (see the discussion following Eq. (B.2)): we have already seen (in Section A.3) that this inverse square distance controls the rate of diffusion from one streamline to another.

Eq. (B.6) is essentially a one-dimensional diffusion equation for $\boldsymbol{W}$ albeit one in a generalised streamfunction space rather than in physical space. The diffusivity varies from streamline to streamline.

Eq. (B.6) does not depend on the Peclet number, but (via the functions D_{eff} and T_{orbit}) does retain dependence on how streamlines are laid out in space. Dependence on Reynolds number is thereby maintained: see Section 4.4.

Eq. (B.6) must be solved in a suitable solution domain, with appropriate boundary/initial conditions (compositions $\boldsymbol{w}^R$ and $\boldsymbol{w}^0$, respectively, as in Section 3.2). Ideally we wish to solve on the domain $t \geq 0$ and $0 \leq \psi \leq \psi_{max}$, where ψ_{max} is the maximum value of the streamfunction (occurring at the internal stagnation point). However, there are technical difficulties with extending the domain all the way to $t \to 0$ and $\psi \to 0$. The streamline orbit time T_{orbit} diverges for $\psi \to 0$ since the poles of the drop are stagnation points. Moreover as was alluded to in Section A.7, for near surface streamlines, and times less than a typical orbit time around such streamlines, replacing the concentration field $\boldsymbol{w}(\psi, s, t)$ by its streamline-average $\boldsymbol{W}(\psi, t)$ will be a poor approximation. On a given streamline at early times, there are some fluid elements which have been in close contact with the drop surface (having a composition near to that on the surface $\boldsymbol{w}^R$), but there are other fluid elements which have passed their entire life in the drop interior (with a composition essentially $\boldsymbol{w}^0$). We require therefore a full numerical simulation (or else a model of the general type discussed in Appendix A) to run up to a small finite time, after which Eq. (B.6) is considered to start to apply: Eq. (B.6) inherits the solute concentration field computed at this small finite time as its initial condition. Likewise the full simulation and/or boundary layer model must identify a particular near surface streamline with a small (but non-zero) ψ value, which has $\boldsymbol{W}$ effectively equal to $\boldsymbol{w}^R$ from the time when Eq. (B.6) starts to apply: Eq. (B.6) is then solved with a boundary condition $\boldsymbol{W} = \boldsymbol{w}^R$ on this streamline, and with a regularity condition at the internal stagnation point $\psi = \psi_{max}$ (as D_{eff} vanishes there).

References

Alonso, L., Arce, A., Francisco, M., Rodriguez, O., Soto, A., 2007. Gasoline desulfurization using extraction with [C_8mim][BF_4] ionic liquid. A.I.Ch.E. Journal 53, 3108–3115.

Bandrowski, J., Kubaczka, A., 1982. On the prediction of diffusivities in multicomponent liquid systems. Chemical Engineering Science 37, 1309–1313.

Batchelor, G.K., 1967. An Introduction to Fluid Dynamics, first ed. Cambridge University Press, Cambridge.

Bird, R.B., Stewart, W.E., Lightfoot, E.N., 1960. Transport Phenomena, first ed. Wiley, New York.

Chambliss, C.K., Haverlock, T.J., Bonnesen, P.V., Engle, N.L., Moyer, B.A., 2002. Selective separation of hydroxide from alkaline nuclear tank waste by liquid–liquid extraction with weak hydroxy acids. Environmental Science and Technology 36, 1861–1867.

Chao, B.T., 1969. Transient heat and mass transfer to a translating droplet. Journal of Heat Transfer, Transactions of ASME 91, 273–280.

Chao, B.T., Chen, J.L.S., 1970. Series solution of unsteady heat of mass transfer to a translating fluid sphere. International Journal of Heat and Mass Transfer 13, 359–367.

Cox, S.J., Weaire, D., Mishuris, G., 2009. The viscous froth model: steady states and the high-velocity limit. Proceedings of the Royal Society A 465, 2391–2405.

Dandy, D.S., Leal, L.G., 1989. Buoyancy-driven motion of a deformable drop through a quiescent liquid at intermediate Reynolds numbers. Journal of Fluid Mechanics 208, 161–192.

Drumm, C., Tiwari, S., Kuhnert, J., Bart, H.J., 2008. Finite pointset method for simulation of the liquid–liquid flow field in an extractor. Computers and Chemical Engineering 32, 2946–2957.

Drumm, C., Attarakih, M.M., Bart, H.J., 2009. Coupling of CFD with DPBM for an RDC extractor. Chemical Engineering Science 64, 721–732.

Einstein, A., 1916. Die Grundlage der allgemeinen Relativitätstheorie. Annalen der Physik 354, 769–822.

Einstein, A., 1905. Zur Elektrodynamik bewegter Körper. Annalen der Physik 322, 891–921.

Goodson, M., Kraft, M., 2004. Simulation of coalescence and breakage: an assessment of two stochastic methods suitable for simulating liquid–liquid extraction. Chemical Engineering Science 59, 3865–3881.

Grassia, P., Montes-Atenas, G., Lue, L., Green, T.E., 2008. A foam film propagating in a confined geometry: analysis via the viscous froth model. European Physical Journal E 25, 39–49.

Green, T.E., Bramley, A., Lue, L., Grassia, P., 2006. Viscous froth lens. Physical Review E 74, 051403.

Handlos, A.E., Baron, T., 1957. Mass and heat transfer from drops in liquid–liquid extraction. A.I.Ch.E. Journal 3, 127–136.

Harrison, C.H., 2006. Multicomponent mass transfer in liquid–liquid extraction. Ph.D. Thesis, School of Chemical Engineering and Analytical Science, University of Manchester, Manchester, UK.

Heinrich, J.C., Huyakorn, P.S., Zienkiewicz, O.C., Mitchell, A.R., 1997. An 'upwind' finite element scheme for two-dimensional convective transport equation. International Journal for Numerical Methods in Engineering 11 (1), 131–143.

Juncu, G., 1999. A numerical study of steady viscous flow past a fluid sphere. International Journal of Heat and Fluid Flow 20, 414–421.

Juncu, G., 2001. Unsteady heat and/or mass transfer from a fluid sphere in creeping flow. International Journal of Heat and Mass Transfer 44, 2239–2246.

Juncu, G., 2005. Unsteady ternary mass transfer from a sphere in creeping flow. International Journal of Thermal Science 44, 255–266.

Klocker, H., Bart, H.J., Marr, R., Muller, H., 1997. Mass transfer based on chemical potential theory: $ZnSO_4/H_2SO_4$/D2EHPA. A.I.Ch.E. Journal 43, 2479–2487.

Kooijman, H.A., Taylor, R., 1991. Estimation of diffusion coefficients in multicomponent liquid systems. Industrial and Engineering Chemistry Research 30 (6), 1217–1222.

Korchinsky, W.J., Grassia, P., Harrison, C.H., 2009. Multicomponent mass transfer in films and rigid drops: the influence of concentration-variable diffusivity. Chemical Engineering Science 64, 433–442.

Krishna, R., Standart, G.L., 1976. A multicomponent film model incorporating a general matrix method of solution to the Maxwell–Stefan equations. A.I.Ch.E. Journal 22, 383–389.

Krishna, R., Standart, G.L., 1979. Mass and energy transfer in multicomponent systems. Chemical Engineering Communications 3, 201–275.

Krishna, R., Wesselingh, J.A., 1997. The Maxwell–Stefan approach to mass transfer. Chemical Engineering Science 52 (6), 861–911.

Kronig, R., Brink, J.C., 1950. The theory of extraction from falling droplets. Applied Science Research A 2, 142–154.

Kumar, A., Hartland, S., 1999. Correlations for prediction of mass transfer coefficients in single drop systems and liquid–liquid extraction columns. Chemical Engineering Research and Design 77, 372–384.

Leal, L.G., 2007. Advanced Transport Phenomena: Fluid Mechanics and Convective Transport Processes. Cambridge Series in Chemical Engineering. Cambridge University Press, Cambridge.

Li, L., Liu, F., Kong, X.X., Su, S., Li, K.A., 2002a. Investigation of a liquid–liquid extraction system based on non-ionic surfactant-salt-H_2O and mechanism of drug extraction. Analytica Chimica Acta 452, 321–328.

Li, T.W., Mao, Z.S., Chen, J.Y., 2002b. Experimental and numerical investigations of single drop mass transfer in solvent extraction systems with resistance in both phases. Chinese Journal of Chemical Engineering 10, 1–14.

Nakano, Y., Tien, C., 1967. Approximate solutions of viscous incompressible flow around fluid spheres at intermediate Reynolds numbers. Canadian Journal of Chemical Engineering 52, 135–140.

Negri, E.D., Korchinsky, W.J., 1986. Multicomponent mass transfer in spherical rigid drops. Chemical Engineering Science 41, 2395–2400.

Negri, E.D., Young, C.H., Korchinsky, W.J., 1986. High flux, single solute mass transfer in spherical rigid drops. Chemical Engineering Science 41, 2401–2406.

Newman, A.B., 1931. The drying of porous solids: diffusion and surface emission equations. Transactions of A.I.Ch.E. 27, 203–221.

Piarah, W.H., Paschedag, A., Kraume, M., 2001. Numerical simulation of mass transfer between a single drop and an ambient flow. A.I.Ch.E. Journal 47 (7), 1701–1704.

Press, W.H., Teukolsky, S.A., Vetterling, W.T., Flannery, B.P., 1992. Numerical Recipes in C. The Art of Scientific Computing, second ed. Cambridge University Press, Cambridge.

Rose, P.M., Kintner, R.C., 1966. Mass transfer from large oscillating drops. A.I.Ch.E. Journal 12, 530–534.

Ruckenstein, E., 1967. Mass transfer between a single drop and a continuous phase. International Journal of Heat and Mass Transfer 10, 1785–1792.

Smith, L.W., Taylor, R., 1983. Film models for multicomponent mass transfer: a statistical comparison. Industrial and Engineering Chemistry Fundamentals 22, 97–104.

Steiner, L., Oezdemir, G., Hartland, S., 1990. Single-drop mass transfer in the water–toluene–acetone system. Industrial and Engineering Chemistry Research 29, 1313–1318.

Stroud, K.A., Booth, D.J., 2001. Engineering Mathematics, fifth ed. Palgrave, Basingstoke, Hampshire (see section 16.53).

Taylor, R., Krishna, R., 1993. Multicomponent Mass Transfer. Wiley, New York, USA.

Toor, H.L., 1964a. Solution of the linearised equations of multicomponent mass transfer. I. A.I.Ch.E. Journal 10, 448–455.

Toor, H.L., 1964b. Solution of the linearised equations of multicomponent mass transfer. II. Matrix methods. A.I.Ch.E. Journal 10, 460–465.

Toutain, J., Le Lann, J.M., Gourdon, C., Joulia, X., 1998. Maxwell–Stefan approach coupled drop population model for the dynamic simulation of liquid–liquid extraction pulsed column. Computers and Chemical Engineering 22, S379–S386.

Uribe-Ramirez, A.R., Korchinsky, W.J., 2000a. Fundamental theory for prediction of single-component mass transfer in liquid drops at intermediate Reynolds numbers ($10 < Re < 250$). Chemical Engineering Science 55, 3305–3318.

Uribe-Ramirez, A.R., Korchinsky, W.J., 2000b. Fundamental theory for prediction of multicomponent mass transfer in single-liquid drops at intermediate Reynolds numbers ($10 < Re < 250$). Chemical Engineering Science 55, 3319–3328.

Vikhansky, A., Kraft, M., 2004. Modelling of a RDC using a combined CFD-population balance approach. Chemical Engineering Science 59, 2597–2606.

van Vliet, R.E., Tiemersma, T.P., Krooshof, G.J., Iedema, P.D., 2001. The use of liquid–liquid extraction in the EPDM solution polymerization process. Industrial and Engineering Chemistry Research 40, 4586–4595.

Waheed, M.A., Henschke, M., Pfennig, A., 2002. Mass transfer by free and forced convection from single spherical liquid drops. International Journal of Heat and Mass Transfer 45, 4507–4514.

Wesselingh, J.A., Krishna, R., 1991. Mass Transfer. Ellis Horwood, Chichester, UK.

Yan, Y., Lai, H., Gentle, C.R., Smith, J.M., 2002. Numerical analysis of fluid flows inside and around a liquid drop using an incorporation of multi-block iteration and moving mesh. Chemical Engineering Research and Design 80, 325–331.

Yang, C., Mao, Z.S., 2005. Numerical simulation of interphase mass transfer with the level set approach. Chemical Engineering Science 60, 2643–2660.

Zimmerman, W.B., 2007. Multiphysics Modelling with Finite Element Methods. World Scientific Publishing Company, Singapore.